European Union

Ministero dell'Istruzione

dellUniversità e della Ricerca

Università degli Studi

di Palermo

Università degli Studi di Palermo

Department of Physics and Chemistry

International PhD Course in Applied Physics

Cycle XXIII 2013

Coordinator: Prof. Bernardo Spagnolo

Application of the chaotic map algorithm in the analysis of biomedical images

PhD student

Marius Mihail IACOMI

Supervisor

Prof. Giuseppe RASO

Acknowledgements

The present thesis is the result of several years of personal work, but it is also the expression of invaluable help and support from the part of my family and the colleagues. This thesis would have remained a dream had it not been for the continuous and valuable support through all these years from the part of my former and present supervisors, prof. Francesco Fauci and prof. Giuseppe Raso whom I deeply thank for their guidance and encouragement in the toughest moments of the work. It is a pleasure for me to recall the fruitful discussions and the important interaction with the members of the team at the Physics Department of the Palermo University where the main activities were performed; particularly, I want to thank to Donato Cascio, Maria Vasile, Rosario Magro and Letizia Vivona for their precious help and suggestions during all these years and for creating a pleasant and positive work ambience.

I thank also prof. Leonardo Angelini from the Bari University, for his insight suggestions concerning the application of the chaotic maps method.

My full gratitude goes to the coordinator of the Doctoral School, prof. Bernardo Spagnolo, for his permanent care, interest and patience.

I am equally grateful to my scientific advisor, prof. Roberto Bellotti from the Bari University, who accepted to referee this thesis and provide useful advices.

To all the teaching staff of the Doctoral School who provided high quality scientific insight on relevant topics go my sincerest thanks for their comprehension and dedication.

I have to mention here the staff of the Physics Department where the research activities were performed: I am very grateful to all of them, with a special thought for the former head of the department, prof. Maria Brai.

I am particularly grateful to my wife, Silvia Ursino, who supported me during all these years with love, encouragement and patience allowing me a successful finish of the work.

For his lifelong attention, I have to thank to my father, Mircea Mihail Iacomi, who played a determinant role in my choice of a scientific career; while this journey has been sadly marked by his passing away before the completion of the work, another life marked it with joyful yet time-consuming occupations after her birth: my daughter Iulia.
This work is dedicated to both of them.

Statement of Purpose (Abstract)

The object of this thesis is the application of a novel clustering approach to the analysis of biomedical images. The chaotic map clustering algorithm is here used for two different purposes within this field. The first one is the segmentation of digital mammographic images, a process of grouping together similar subsets of image pixels resulting in a medically meaningful image partition. The image is divided into pixels subsets characterized by a set of conveniently chosen features and each of the corresponding points in the feature space is associated to a map. A mutual coupling strength between the maps depending on the associated feature space points distance is subsequently introduced. On the system of maps, the simulated evolution through chaotic dynamics leads to its natural partitioning, which corresponds to a particular segmentation scheme of the initial mammographic image. The significance of the results obtained and the applicability of the proposed method as preliminary step in automatic flows is discussed. The second application field is the pre-classification step in the analysis of indirect immunofluorescence images, a process aiming to the assignation of input images to a class from a given set. The images themselves are characterizable by an appropriate set of features which determine their corresponding points in the data space. For an input set consisting of a significant number of known type images and one unknown type image, each corresponding point gets associated with a map in interaction with its map neighbours according to a given distance law. Subsequently, the maps are let to evolve through chaotic dynamics and their final clustering scheme into a given number of classes provides a classification for the input unknown image. The applicability of the results obtained in an automatic work flow is subsequently analyzed. The thesis concludes with some overall considerations about the use of chaotic map clustering algorithm in the analysis of biomedical images.

Contents

Chapter 1

Chaotic map clustering

1.1 Clustering overview

1.1.1 Clustering generalities

Clustering represents the task of partitioning a set of objects into a number of groups so that objects belonging to a same group (which is called cluster) are more similar (in some sense, depending on the examined problem and its particular implementation) than to the objects from other clusters. Therefore, the partition clustering subsets find a meaning in the context of a specific problem. Although the cluster analysis can be seen as a way of classifying objects into meaningful subsets, clustering has not to be confused with common classification techniques normally characterized by assigning the objects to a restricted set predefined classes [1]. Clustering techniques are basically used for data mining and they find various fields of application such as machine learning [2], pattern recognition [3], pattern classification [4], image analysis [5], information retrieval [6], bioinformatics/genetics [7], communications [8], speech recognition [9], high-energy physics [10], astrophysics [11], finance/business [12], analysis of dynamical systems [13], to cite only some of them.

Cluster analysis itself is not synonymous of a given algorithm, but a general machine

learning problem to be solved. The generic task can be performed through the application of various algorithms significantly different in which concerns the clusters definition and the ways of their efficient finding. Usual cluster definitions include basically those groups characterized by low distances among the objects members of a cluster, but also regions of increased density in the data space, intervals or some particular statistical distributions. There are no universal appropriate clustering algorithm and parameter configuration scheme (including values of parameters such as the specific distance function, the density threshold or the total number of clusters): the choices depend on the characteristics of the individual data set and (in a lesser extent) on the intended use of the results. Therefore, clustering does not reduce to a completely automatic classification task, but an complex process of optimization involving trial and failure. Achieving the desired results will often imply significant adjustments of the algorithm and its parameters.

The clustering problem is intrinsically ill-posed: the inherent difficulty of the cluster analysis arises from the ambiguity of decision concerning what a cluster is. The clusters to be established depend on the total number of partition subsets and the desired resolution in the data space, and these parameters are determined for each particular problem.

1.1.2 Data representation in clustering

In order to perform an efficient cluster analysis, the input data must be appropriately represented [14]. Assuming a distance-based characterization of data, the corresponding clustering algorithms have to match data type and to correctly incorporate the aspects of scale, normalization and proximity measure types.

Let the analyzed set consist of n objects represented as points (vectors) in a d-dimensional (feature) space. The set is thus organized in a $n \times d$ *pattern matrix*: the rows of the matrix identify the pattern (object) while the columns denote the *features* which measure the objects. Most commonly, the d features lay on a set of orthogonal axes, justifying the use of the mathematical term "space". One can represent a cluster

as a subset of points/patterns close to one another or satisfying an appropriately chosen spatial relationship. While visual representations are limited to two or three spatial dimensions, cluster analysis allows the organizing of multidimensional data beyond our physiological limitations.

The "must" ingredient of all distance-based clustering methods is the *proximity index* between pairs of objects. This parameter is a measure of the affinity of the considered objects and is usually computed from the pattern matrix. The proximity indices are naturally organized into a usually symmetric $n \times n$ dimensional matrix called the *proximity matrix*. The affinity measure can be expressed either as *similarity* (e.g. the correlation coefficient) or *dissimilarity* (e.g. the Euclidean distance between points).

The features characterizing data points are here conveniently assumed to be *continuous* (the other possibilities, *binary* and *discrete* features, are of lower interest and are mentioned only for the sake of conformity); therefore, only numerically meaningful features will be considered in the following. Consequently, one can generate continuous data in the proximity matrix ranging on a ratio quantitative scale.

Let the column vector $\mathbf{x}_i = (x_{i1}\, x_{i2} \ldots x_{id})^t, i = \overline{1,n}$ denote the ith pattern in the pattern matrix. Any kind of *metric* defined on the feature space defines a dissimilarity matrix, $[d(i,j)]$, where i and j label the representative points of the objects in feature space. In particular, one may consider the generic weighted Minkovski metric,

$$d(i,j) = \left(\sum_{k=1}^{d} w_k^r |x_{ik} - x_{jk}|^r \right)^{1/r} \quad (r \geq 1) \tag{1.1}$$

as a valid possibility for generating a dissimilarity matrix from the pattern matrix. The most common cases of used metric are obtained for $r = 2$ (usual Euclidean distance), $r = 1$ (the Manhattan distance) or $r \to \infty$ (the so-called "sup" distance). A non-trivial example is the Mahalanobis *generalized distance* defined as:

$$d(i,j)^2 = (\mathbf{x}_i - \mathbf{x}_j)^t \mathbf{W}^{-1} (\mathbf{x}_i - \mathbf{x}_j) \tag{1.2}$$

where $\mathbf{W}$ is the pooled within-group covariance matrix for the two groups to which belong

the points $\mathbf{x}_i$ and $\mathbf{x}_j$ (see e.g. [15]). While the features are automatically standardized to zero mean and unit variance, this scheme has a major drawback in a clustering context: the assignation of the points to a particular cluster has to be done *a posteriori*.

As a similarity measure, one could take here the Pearson linear correlation,

$$\phi_{ij} = \frac{\sum_{k=1}^{d} w_k (x_{ik} - \overline{x}_i)(x_{jk} - \overline{x}_j)}{\left[\sum_{k=1}^{d} w_k (x_{ik} - \overline{x}_i)^2 \cdot \sum_{k=1}^{d} w_k (x_{jk} - \overline{x}_j)^2\right]^{1/2}} \quad \text{with} \quad \overline{x}_i = \sum_{k=1}^{d} w_k x_{ik} / \sum_{k=1}^{d} w_k \tag{1.3}$$

and one could define also a corresponding dissimilarity measure through $\delta_{ij} = (1 - \phi_{ij})/2$ (one has $-1 \leq \phi_{ij} \leq 1$, with 1 indicating the strongest possible positive relationship, while -1 standing for the strongest possible negative relationship. The use of this kind of coefficient is plagued by some drawbacks within a clustering context. A simple and general similarity measure has been proposed by Gower ([16]):

$$s_{ij} = \sum_{k=1}^{d} w_{ijk} s_{ijk} / \sum_{k=1}^{d} w_{ijk} \quad \text{with} \quad s_{ijk} = 1 - |x_{ik} - x_{jk}|/R_k \tag{1.4}$$

where w_{ijk} are either significance or weight coefficients and R_k is the observational range of the k^{th} feature over the set of objects representative points.

Data normalization is usually performed on the input "raw" data in order to increase significance of different features comparison. In fact, the use of Euclidean distance as dissimilarity index automatically grants a privileged role for the large-ranged features over the small ranged ones. One can overcome this problem by an appropriated normalization scheme. Let's denote the original "raw" feature values with an asterisk: thus, the unnormalized j^{th} feature of the i^{th} pattern will be denoted with x^*_{ij}. We define the j^{th} feature average over the set of points

$$m_j = \frac{1}{n} \sum_{i=1}^{n} x^*_{ij} \tag{1.5}$$

and the j^{th} feature variance

$$s_j^2 = \frac{1}{n} \sum_{i=1}^{n} (x^*_{ij} - m_j)^2 \tag{1.6}$$

The most common normalization scheme translates and scales the features in order to reduce them to zero mean and unit variance:

$$x_{ij} = \frac{(x^*_{ij} - m_j)}{s_j} \tag{1.7}$$

This normalization scheme is used also in the present work.

1.1.3 Clustering algorithms

The clustering can be performed through using a certain algorithm. In the literature one can find many different clustering algorithms which are used to solve particular problems. In the following, a brief classification sketch of the classification/clustering algorithms is given.

a) A first classification of the algorithms distinguishes between *exclusive* and *non-exclusive* schemes. In the exclusive classifications, each object belongs strictly to one subset, while in non-exclusive classifications this constraint is not fulfilled. Non-exclusive methods can be *overlapping* (if an object can definitely belong to more than one class) or *fuzzy* (if an object belongs to every cluster with a membership weight ranging between 0 and 1, which can be also be interpreted in terms of clusters being fuzzy sets). While non-exclusive methods are of interest in certain particular cases, most clustering schemes univocally assign the objects to single clusters. The classifications examined below concern only exclusive algorithms.

b) The exclusive algorithms are divided into *supervised* (extrinsic) and *unsupervised* (intrinsic). The supervised algorithms use prior knowledge about the objects to be partitioned (e.g. the number of classes, the assignment of the points to a certain class) and many authors distinguish these methods from "true" cluster analysis which is referred to as "unsupervised classification" [17]. The unsupervised algorithms use exclusively the information contained in the proximity matrix to perform the classification task and makes no use of a priori knowledge about the final partitional classes.

c) The (exclusive) unsupervised algorithms are further subdivided into *hierarchical* and *partitional* methods. This is the main distinction criterion among various clustering algorithms. Hierarchical classification makes use of a nested sequence of partitions obtained from the proximity matrix and cluster identification occurs through a recursive-type method (which may be *agglomerative* or *divisive*). Partitional classification algorithms generate directly the final partition of the data, with the aim of recovering the natural groups which the data consists of.

d) The classification algorithms can be also subdivided into *parametric* and *nonparametric*. Parametric algorithms make use of assumptions about the final structure of the clusters (e.g. point density, distribution of points in the cluster around its center) and a clustering criterion function taking an extremal value for the optimal classification, while nonparametric methods make no such assumptions and do not define any explicit function giving cluster separation in the data space. The objective of a parametric classification method is to find the clustering scheme which leads to the extremal (usually minimal) value for the minimization criterion; some classical examples of parametric approaches are variance minimization, maximal likelihood, and fitting Gaussian mixtures. If there is no a priori knowledge about the final cluster data structure, nonparametric approaches suit better the analyzed particular problem. The main drawback of nonparametric approaches is the lack of cluster validity criteria; other critical issues characterizing these techniques are the lack of a straightforward way to determine which the most significant partitions among the final hierarchy and their tendency to create clusters even when the data does not contain any natural clusters.

Popular classification/clustering algorithms include K-means, connectivity-based (hierarchical), density-based, etc. The choice of a "right" clustering algorithm for a given problem is not an easy task and there is no easy way to determine if a particular classification method will reveal itself efficient or not.

1.2 Chaotic Map Algorithm

1.2.1 Introduction

Towards the end of the last century, a new promising nonparametric method of clustering relying on the physical properties of the inhomogeneous Potts model has been proposed by Blatt, Wiseman and Domany [18], [19]. They restated the data clustering task in terms of measuring the equilibrium properties of the mentioned model; by solving the physics of the inhomogeneous ferromagnetic system they were able to obtain good clustering solutions. The proposed method exhibits a series of advantages rather unique: it naturally generates information about the different data self-organizing regimes, the final number of clusters is provided as an algorithm output, and the hierarchical data structure is represented by merging or splitting of the clusters at the variation of a control parameter (the physical temperature). Additional positive features of the method are, the insensitivity of the results with respect to the initial conditions, robustness of the algorithm against the presence of noise, and computational efficiency. The ferromagnetic Potts model is a system of individual spins described by the parameter $s \in \overline{1,q}$ with $q > 1$, located on the sites of a lattice and whose mutual interaction is described by a non-vanishing strength J_{ij} associated to the couple of neighbor points i and j (subsequently denoted by $< i, j >$) if $s_i \neq s_j$. The Hamiltonian of such a system,

$$\mathcal{H}(s_k) = \sum_{<i,j>} J_{ij}(1 - \delta_{s_i,s_j}) \tag{1.8}$$

is essentially similar to the energy functions used in other spin and neural systems. The homogeneous Potts model (characterized by equal nearest-neighbor couplings $J_{<i,j>} = J$) exhibits two phases: paramagnetic disordered at high temperature, ferromagnetic ordered at low temperature; this model is easily described by statistical means and is of low interest for the clustering issue. The strongly inhomogeneous Potts models are characterized by the formation of magnetic "grains" within which the interactions between neighbors are strong while couplings between all other pairs are very weak. These models also ex-

hibit a ferromagnetic ordered phase at low temperatures and a paramagnetic disordered phase at high temperatures; in addition, at intermediate temperatures the models present a superparamagnetic phase characterized by alignment of spins in strongly coupled grains and no relative ordering of different grains. The superparamagnetic regime is best reflected by the system's magnetic susceptibility, χ: the transition from ferromagnetic to superparamagnetic is accompanied by a noticeable peak of χ, the superparamagnetic phase is characterized by large fluctuations in the magnetization and susceptibility, while at the reaching the full paramagnetic regime, the susceptibility decreases abruptly. The characterization of the superparamagnetic regime accounts for the breaking of the grains clusters into macroscopic subclusters at the raising of the temperature: thus, the superparamagnetic phase itself naturally displays a hierarchical behavior.

The generic inhomogeneous ferromagnetic Potts model can be used for clustering purposes according to the following scheme (see e.g. [19]):

1. Construct an associated physical Potts spin problem
   - *a*) Associate a Potts spin variable $s_i \in \overline{1,q}$ to each pattern vector $\mathbf{x}_i$
   - *b*) Construct a system of neighbors for each pattern vector $\mathbf{x}_i$
   - *c*) For each couple of neighboring points $< i,j >$ calculate the coupling $J_{ij} \propto \exp\left(-\frac{\|\mathbf{x}_i - \mathbf{x}_j\|^2}{2a^2}\right)$
2. Locate the superparamagnetic phase regime
   - *a*) Compute average magnetization $< m >$ and susceptibility χ for different temperatures
   - *b*) From analysis of χ, establish the temperature limits of the superparamagnetic regime
3. Construct the data clusters at the superparamagnetic regime
   - *a*) Measure the mutual spin correlation G_{ij} for all neighboring couples $< i,j >$
   - *b*) From correlation data, construct the data clusters

which already contains several key characteristic elements in common with chaotic map approach, the central feature being the change from the original problem similarity index (representative points mutual distance $\|\mathbf{x}_i - \mathbf{x}_j\|$) to the more flexible spin-spin correlation

function $\langle \delta_{s_i,s_j} \rangle$.

About at the same time, a mostly similar clustering property expressed in terms of chaotic dynamical networks was described by Manrubia and Mikhalkov [20]. With respect to the physics of the Potts model, their model introduces two new crucial elements: an associated dynamical system of maps with chaotic behavior and the phenomenon of mutual synchronization among the maps. Their dynamics of the (randomly coupled) maps is defined as:

$$x^i(t+1) = \left(1 - \frac{\varepsilon}{\nu}\frac{1}{n-1}\sum_{j=1}^{n} T_{ij}\right) f(x^i(t)) + \frac{\varepsilon}{\nu}\frac{1}{n-1}\sum_{j=1}^{n} T_{ij} f(x^j(t)) \qquad (1.9)$$

where the couplings are characterized by the symmetrical random matrix $[T_{ij}]$ (with $T_{ii} = 0$), the average connectivity is given by

$$\nu = \frac{1}{n(n-1)}\sum_{i,j=1}^{n} T_{ij} \ , \qquad (1.10)$$

the parameter ε constrained by $\varepsilon < \nu$ measures the scale of coupling intensity and $f(x)$ is the individual map function (subsequently chosen by the authors as the standard logistic $f(x) = 1 - ax^2$). The equation (1.9) with (1.10) may describe also the limiting case of globally coupled maps whose chaotical dynamics was thoroughly investigated by K. Kaneko ([21]-[28]). Manrubia and Mikhalkov operate a comparison of the behaviors of globally and randomly coupled maps from the point of view of clusters formation in the system of maps. As well as in the case of the Potts model, the system exhibits several phase transitions at the varying of a parameter (here: the coupling strength ε), the globally coupled maps system exhibiting a wider set of phases compared with the system of randomly coupled maps. The dynamical behavior of the systems reflecting also cluster dynamics is described through the use of several parameters; of particular interest is the use of the mutual information between two maps as a measure of their mutual correlation degree.

Combining the change of the analyzed system present in the Blatt, Wiseman and Domany approach with the better suited dynamical system considered by Manrubia and Mikhalkov

yields to a very flexible nonparametric partitional clustering method with a system of chaotic maps in interaction which is presented in the following.

1.2.2 Chaotic Maps essentials

A *map* is a discrete-time *dynamical system* defined as an ordered list of elements $(\mathbb{Z}, M, f)$, where $\mathbb{Z}$ are the integers, M is a manifold locally diffeomorphic to a Banach space and $f : M \to M$ is a continuous function. As for any other dynamical system, the map is essentially characterized by its *evolution* in "time"; in most cases, the integer set where "time" takes the values actually reduces to the natural numbers $\mathbb{N}$ and the "functioning" of the map is given by the recursive relation

$$x_{i+1} = f(x_i) \quad (\text{with } x_k \in M \ \forall k \in \mathbb{N}) \tag{1.11}$$

Very often, the dynamical system is identified with the deterministic mathematical rule generating his time evolution, so for a loose definition one might take into consideration only this prescription and state that the map itself is given by (1.11) (see e.g. [29] or [30]). Thus, from an initial state of the system (x_0) one can univocally deduce the sequence of states of the system at any subsequent time $t \in \mathbb{N}$ by repeated application of (1.11). The space where the manifolds are embedded can be referred to as *phase space*, while the sequence of states reached by the system in its dynamical evolution and contained in the phase space is usually called *orbit* or *trajectory*. If the orbit exhibits a non-periodical, apparently "unpredictable" behavior, the dynamical system (in particular: the map) may be labeled as *chaotic*. The main indication of the chaotic behavior is the strong (on a short term: exponential) orbit dependence on initial conditions. Here are listed several other properties of chaotic systems:

1. Chaos results from deterministic nonlinear processes whose mechanism results from stretching and folding;

2. Chaotic orbits remain bounded within the phase space;

3. Chaotic orbits have a broadband power spectrum because a chaotic orbit consists of unstable orbits of all periods;

4. Chaotic attractors often exhibit fractal properties;

5. Chaotic systems generally follow certain routes to chaos following the variation of some control parameter.

An useful quantitative measure of chaos is the *Lyapunov exponent*: this parameter measures the divergence rate of nearby orbits after averaging over the chaotic attractor. For a bounded system, the chaotic behavior corresponds to a positive and finite Lyapunov exponent. The Lyapunov exponent can be defined by examining the exponential separation growth rate between two neighbor orbits after a number of iterations. If the initial states of the neighbor orbits are x_0 and $x_0 + \varepsilon$, the separation of the orbits after N iterations can be written as

$$|f^N(x_0 + \varepsilon) - f^N(x_0)| = \varepsilon\, e^{N \cdot \lambda(x_0)} \tag{1.12}$$

where $\lambda(x_0)$ is the Lyapunov exponent. A more correct formal expression for this exponent is deduced from (1.12) by taking the limits $\varepsilon \to 0$ and $N \to \infty$:

$$\lambda(x_0) = \lim_{N\to\infty} \lim_{\varepsilon\to 0} \frac{1}{N} \log \frac{|f^N(x_0 + \varepsilon) - f^N(x_0)|}{\varepsilon} = \lim_{N\to\infty} \frac{1}{N} \log \left| \frac{df^N(x_0)}{dx_0} \right| \tag{1.13}$$

One has to mention here the simplest nonlinear difference equation map used within this context, the logistic;

$$x_{n+1} = r x_n (1 - x_n) \tag{1.14}$$

where the parameter $r \in [0, 4]$ and $0 \leq x_k \leq 1$. The behavior of the logistic map allows one to distinguish between the so-called "bifurcation regime" for $1 < r < r_\infty$ characterized by negative values of the Lyapunov exponent λ and the "chaotic region" for $r_\infty < r \leq 4$ where one has mostly an exponent $\lambda > 0$ (in this region there are also a series of intervals in r where $\lambda < 0$ and the corresponding orbits are still periodic). For this map, the shift from periodicity to chaos occurs at $r_\infty = 3.5699456\ldots$.

1.2.3 Chaotic Maps Clustering Algorithm

As previously hinted, the chaotic dynamic systems can be used for practical clustering purposes. The use of the chaotic maps for the clustering of pattern systems representative points in the feature space has been formalized and advocated since early 2000's by the work group lead by prof. Angelini from the Bari University ([31]-[37]). During the last decade, a series of successful various applications of this clustering method emerged in the literature, applications such as landmine detection [32], EEG signals analysis in medicine [33], gene analysis in biology [34] or financial analysis (stock markets [35], financial time series [36]).

Within this approach, a chaotic map system is associated to a given data set in such a way that the structure of this last one is reflected in the cluster formation of quasi-synchronized maps. The method relies on the cooperative behavior of the coupled chaotic maps whose dynamics naturally leads to cluster groups of synchronized maps on similar orbits. The algorithm uses the mutual information as similarity index for performing a hierarchical data clustering, without any further assumption on the number of clusters and their density distribution.

The algorithm can be applied to any situation describable through the means of a numerical features set. Let d denote the number of features and n the number of objects to be classified. For each object one may compute the values of the d features and associate a representative point in the corresponding feature space. The set of representative points is

$$\mathbf{R} = \left\{ \mathbf{r}_i | i \in \overline{1,n} \right\} \tag{1.15}$$

where the vector $\mathbf{r}_i = (r_{i1} r_{i2} \dots r_{id})^t$. This set is further mapped in a system of maps in interaction. The matrix element characterizing the interaction between the points i and j is defined as

$$J_{ij} = \exp\left[-\frac{(\mathbf{r}_i - \mathbf{r}_j)^2}{2a^2} \right] \tag{1.16}$$

where a is a local length scale parameter. The dynamical variable of each map is real and bounded, $x_i \in [-1, 1]$ and its (discrete) time evolution is given by:

$$x_i(t+1) = \sum_{i \neq j=1}^{n} J_{ij} \; f(x_j(t))/C_i \tag{1.17}$$

In the relation (1.17), the coefficients C_i are normalization constants defined as $C_i = \sum_{i \neq j=1}^{n} J_{ij}$, and the function f is the particular logistic map, $f(x) = 1 - 2x^2$, constructed such as to map the interval $[-1, 1]$ on itself, for the highest possible value of the parameter, a choice which ensures the chaotic regime for each map. Incidentally, one can note that the variable change $y = f(x)$ allows rewriting the dynamics (1.17) in a form more similar to the evolution equations occurring in the field of neural networks:

$$y_i(t+1) = f\left(\frac{1}{C_i} \sum_{i \neq j=1}^{n} J_{ij} \; y_j(t)\right) \tag{1.18}$$

where f plays the role of a transfer function. The local scale a appearing in (1.16) is estimated as average distance of the K-nearest neighbors, where K is the only surviving free parameter of the algorithm. While the choice of this parameter is somehow arbitrary, the results should not exhibit an important dependence on its particular value ([31]). Within this context, the points i and j are nearest neighbors if and only if the point i is one on the K nearest neighbors of j and conversely, the point j is one of the K nearest neighbors of i.

During the evolution phase, the individual orbits are chaotic but the maps whose nearest neighbors are similar will synchronize through their interactions (contained in J_{ij}). After a conveniently chosen number of temporal steps T, the synchronized evolution of the similar maps can be easily detected. In order to check the correlation properties of the whole system of maps, one introduces an auxiliary temporal sequence of sign bits for each map $S_i(t)$ defined as following:

$$S_i(t) = \begin{cases} 1 \text{ if } x_i(t) > 0 \\ 0 \text{ if } x_i(t) \leq 0 \end{cases} \tag{1.19}$$

From the sequence of bits one can compute the *Shannon entropy* for the i^{th} map:

$$H_i = -\sum_{b=0,1} P_i(b) \ln P_i(b) \tag{1.20}$$

where $P_i(k)$ is the probability of occurrence for the bit b in the sequence $\left\{S_i(t)|t \in \overline{1,T}\right\}$ defined as the ratio of the total number of occurrences of the bit b to the total number of bits in the sequence, T. In an analogous manner one can compute the *joint entropy* for any couple of maps $\{i,j\}$ with $i \neq j$:

$$H_{ij} = -\sum_{b_i=0,1} \sum_{b_j=0,1} P_{ij}(b_i,b_j) \ln P_{ij}(b_i,b_j) \tag{1.21}$$

where $P_{ij}(b_i,b_j)$ is the probability of incidence of $\{S_i(t),S_j(t)\} = \{b_i,b_j\}$ in the temporal sequences of bits.

The good measure of the synchronism is the mutual information between the maps $\{i,j\}$ ([38])which can be simply obtained from (1.20) and (1.21) as

$$I_{ij} = H_i + H_j - H_{ij} \tag{1.22}$$

For completely synchronized maps, the sequences of bits are identical, therefore $H_i = H_j = H_{ij}$ and the mutual information reaches its maximum value (in our case, this maximum is $\ln 2$ due to the choice of the function f). Non-synchronized maps have completely independent sequences of bits, therefore one has $H_i + H_j = H_{ij}$ and the mutual information vanishes as expected.

The final step of the algorithm is the cluster extraction. The mutual information of the couples of maps defines a kind of "topology" which can be used for the construction of a hierarchy of groups. The construction of the clusters is realized in two steps:

- all the couples of maps for which the mutual information exceeds a threshold value ($I_{ij} > \theta$) are considered graph-connected, while if $I_{ij} < \theta$ the points i and j will have no direct connection;

- once all the connections between the couples of maps have been set, the clusters result as connected parts of the graphs previously obtained. In other words, two maps belong to a same cluster if there exists a path of mutually connected maps joining them.

Within this approach, the threshold θ lays obviously between 0 and $\ln 2$. In particular, for $\theta = 0$, all the points are connected in an unique big cluster, while for $\theta = \ln 2$ every point in the feature space belongs only to its own cluster[1]. In between these extremes, one has to find the "best" partition scheme.

The number of clusters monotonically increases with the threshold and their hierarchy is naturally obtained from the graph's increasing connectivity. A particular clustering scheme is arguably meaningful if the clusters are stable under the variation of the threshold; the stability conditions can be quantized as follows:

- the number of clusters is stable over a significant θ variational range;
- the size of the biggest clusters is not affected by variation of θ on a significant range.

These conditions are strong indications that the clustering scheme obtained through application of the algorithm is not a spurious artifact of meaningless numerical output but it rather reflects some deeper similarity property of the input data. In the above figure (1.1) an illustrative result of the hierarchical clustering with the threshold method is represented.

[1] with the noticeable exception of the points perfectly synchronized from the very beginning

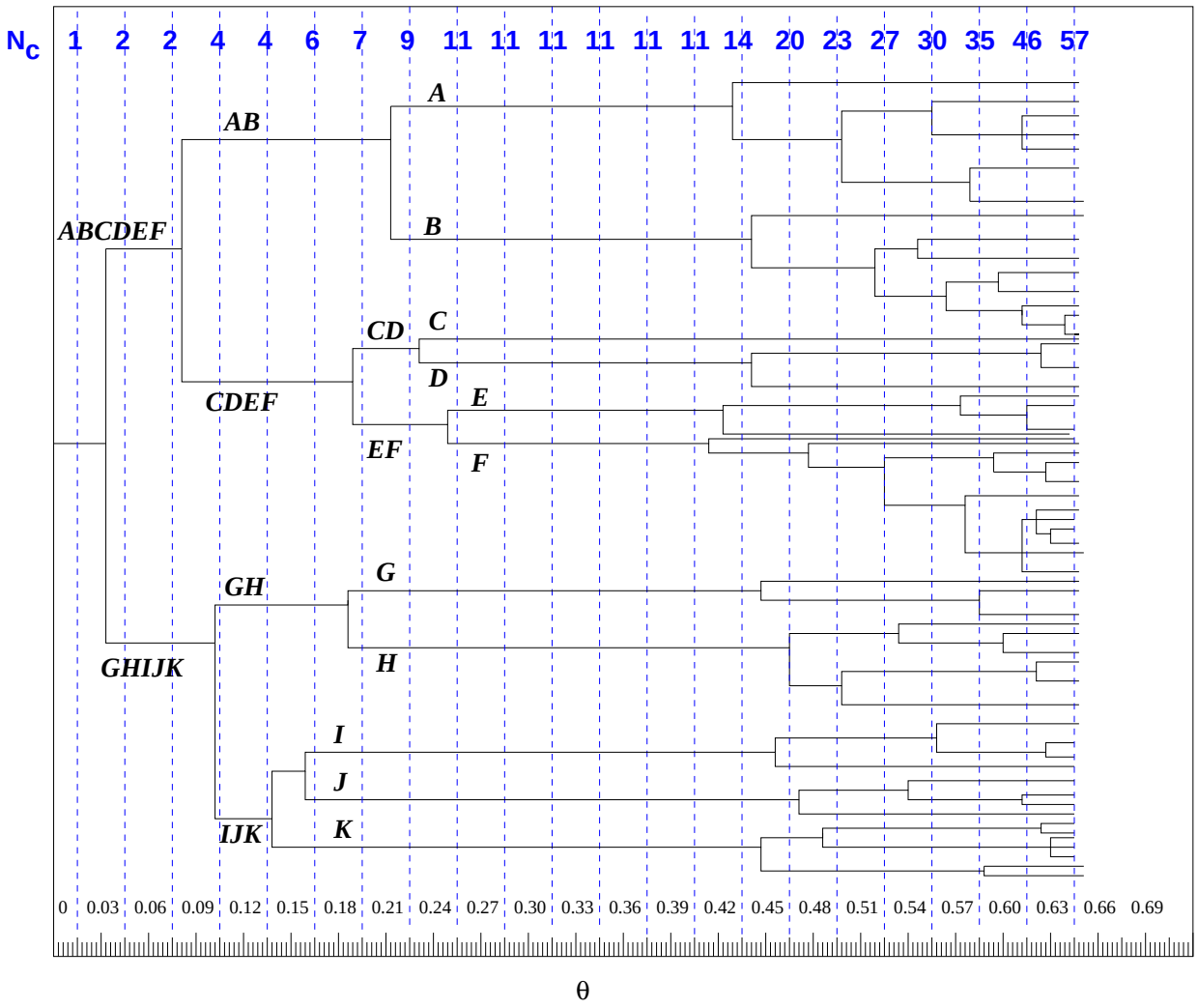

Figure 1.1: Illustrative dendrogram for hierarchical clustering. The most stable portion corresponds to the range $0.25 < \theta < 0.41$; the 11 most meaningful clusters are labeled with letters from A to K. For larger values of θ the number of clusters N_C increases gradually faster as the clusters split over and over and approaches the number of input points with $\theta \to \ln 2$

Chapter 2

Mammographic images segmentation

2.1 Introduction

2.1.1 Mammography overview

At present, breast cancer is still the most common cancer among women, apart the cancers of the skin, and one of the main female cancer death causes ([39], [40], [41]). The most widely used method for detecting breast cancer in its early stages is the mammography, a technique which has lately taken advantage of the supplementary features offered by the digital format [42]. Mammographic modality makes use of the mammograms – X-ray images of the breast which contain visual information about the potential pathologies inside the breast. The tissue components of the breast attenuate in a greater or lesser degree the X-ray beam according to their interaction properties, and the output image is nothing but record of these interactions. The X-ray are usually differently attenuated by malignant tissues than by normal breast parenchyma, and the result of this differentiation can be detected on the mammogram. At present, mammography is still the only breast imaging modality which is documented to have a sensible impact of reducing breast cancer mortality when used within a screening program ([43], [44]). Mammographic screening is aimed to find as many early stage non-invasive or small-sized invasive breast pathologies

as possible, in order to eliminate as many negative consequences as possible through adequate medical treatment. Among the many factors on which depends the effectiveness of a screening program, one can mention the quality improvement of the mammogram reading which is arguably linked to the use of specific auxiliary techniques. During the last decades, along with the digital revolution, the automatic detection of pathologies in the mammographic images has became a widespread auxiliary technique in radiology and the CAD (Computer Aided Detection) systems have proven a certain degree of effectiveness mostly as a second reader (see e.g. [45], [47], [50] or [48]). While an ultimate assessment about automatic systems performance with respect to the correct identifying and hinting out of pathologies is yet to be made, it looks safe enough to predict the increasing importance of these techniques in mammography [46].

2.1.2 Mammographic images segmentation

In the process of automatic searching of pathologies in the images, the partitioning of the image itself in medically meaningful components (homogeneous with respect to one or several appropriately chosen characteristics) is usually a compulsory primordial mid-level step in the processing workflow ([39],[49],[50]):

This phase plays a crucial role: any non segmented lesion at this stage will be irremediably lost for any further analysis. While a wide variety of segmentation approaches have been proposed, there is no standard algorithm that can ensure high levels of significance for all imaging applications ([51], [52]), and the segmentation method has to rely on specific testing on an actual database [53]. In particular, the segmentation of the mass lesions in mammographies is still a challenging task since the masses are usually embedded and obscured by surrounding normal breast parenchyma ([39]) and deciding whether a dense area of the breast in an image represents a true mass lesion or it is just normal parenchyma has been classified as "probably, the most difficult task in reading mammograms" [54]. The segmentation methods proposed in mammography and more

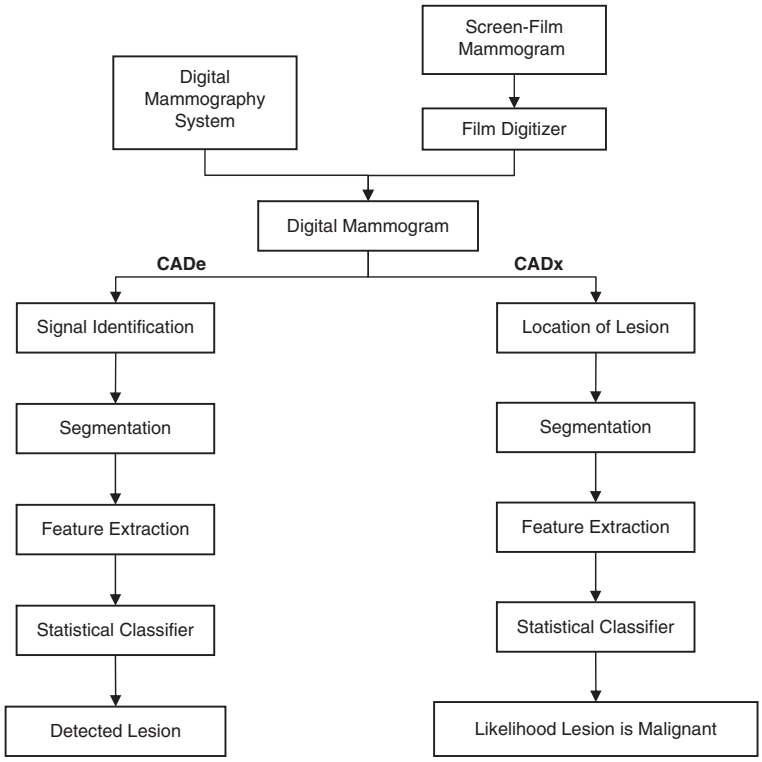

Figure 2.1: Generic flowchart of CADe (detection) and CADx (diagnosis) automatic systems according to Nishikawa [50]. Both branches include the segmentation step.

generally in medical imaging are quite various; for a review see e.g. [55], see also [56] for a particular example. Pham, Xu and Prince identify eight categories of segmentation methods [57]:

1. thresholding approaches
2. region growing approaches
3. classifiers
4. clustering approaches
5. Markov random field models
6. artificial neural networks
7. deformable models

8. atlas-guided approaches

Among these, one of the standard generic segmentation approaches proposed more than three decades ago is the (feature-based) clustering method [58], which associates to each pixel or group of pixels from the image a set of appropriately chosen numerical parameters and transforms the primary segmentation task in a derived clustering problem in the associated feature space. Thus, the process of feature clustering becomes the crucial part of the segmentation algorithm. The main advantage of this approach is that the method does not require the use of a training set [59]. In the above-mentioned paper ([57]) three main clustering algorithms in segmentation are refered: K-means (ISODATA), fuzzy c-means and expectation-maximization. Along with these widely-used algorithms one may group the feature clustering with coupled chaotic maps which is examined in the present thesis.

2.2 Materials and methods

2.2.1 Mammographic images

Most patient cases in mammography come along with the standard four images, two views for each breast: usually, one view from above the horizontally-compressed breast – the craniocaudal (CC) view –, and another from an oblique or angled view with respect to a diagonally-compressed breast – the mediolateral oblique (MLO) view. The two-view system allows the radiologist to gain a 3D representation of the breast. Occasionally, additional views can be recorded for supplementary information (e.g. lateromedial LO, or mediolateral ML). The images are gray shaded so that every pixel is fully characterized by an unique intensity parameter.

The mammographic image reference database used for this work consists of a group of 46 selected cases for a total of 268 images. More specifically, there were considered three distinct datasets: a first set of 24 digitally acquired cases on a GE Senograph 2000D containing 98 images, a second set of 22 digitalized cases on a Fuji CR mammograph containing 97 images; moreover the segmentation algorithm was also tested on a third set of 73 anonymized images containing micro-calcifications clusters digitally acquired on a Lorad Selenia Full Field Digital Mammograph. All the digitally acquired images were subsequently stored on a PACS system. The eventual pathologies have been diagnosed and classified by two expert senior radiologists; all diagnosed pathologies have been further confirmed by histological examination. Each image of this database has been separately submitted to an independent segmentation process.

The mammogram typical sizes range from about 1000×1800 pixels to 2048×2560 pixels, corresponding to a maximum of 5242880 points characterized by their individual gray level. The images gray levels are coded either on an 8-bit or a 12-bit scale. The resolution of a mammogram is usually of about 80μ per pixel.

2.2.2 Specificities of CMC algorithm implementation

The implementation of the Chaotic Maps algorithm for the analysis of mammograms can be roughly divided in three different phases: maps system initialization, evolution of the system of maps and the analysis of temporal sequences obtained.

In the **initialization phase**, most basic choices are performed. The input image has to be mapped in terms of points in a feature space to be clustered by the chosen algorithm. Subsequently, it's still at this stage that to each point in the feature space one has to associate a map and compute its mutual interaction coefficients J_{ij} in the matrix 1.16. Since no a priori information about the image pixels is available, for the first step the mammographic image has to be partitioned in squares (the most natural choice of a regular partitional pattern) small enough to match the typical dimensionality of the smallest objects of interest for the radiologist and enough rich in pixels in order to enable the computing of relevant associated features. It turns out that a choice of the square side around 20 pixels is enough to get meaningful values for the statistical features (with 400 input points for each square) and small enough (about $1,6mm$ in real size) to match the small micro-calcifications typical sizes. Values inferior to 20 for the elementary size bring little in terms of partition resolution but a heavy increase of the computational needs. Therefore, for each elementary unit a vector of features is computed leading to an associated point in the feature space.

Due to the fixed geometry of the initial partitioning, no geometrical or form-based feature can be taken into account at this stage. This aspect is very penalising especially for the masses lesions which are usually characterized not only by density but also by shape and contour type: the classic appearance of a breast pathology in a mammogram is *an irregular mass, often with ill-defined or spiculated margins* ([60]; see also [61], [62]). The features used to characterize elementary units are the usual statistical central moments

(mean pixel gray value, variance, kurtosis, skewness) and several autocorrelation values (energy, entropy, contrast) accounting for the texture ([59]; for the generic texture features see also [63], [64]).

The position of the square in the image has a definite importance: any segmented lesion should be a contiguous region composed of one or several groups of pixels, therefore any medically meaningful clusters of points in the data space have to correspond to spatially connected groups of neighbor squares in the image. Hence, it results necessary to treat separately the positional feature as a compulsory check.

A particular attention has to be paid to the region outside the breast: this area contains only essentially black pixels and computing features on it yields not only an useless extra computational charge but also a potentially confusing set of points in the feature space which would affect the feature distribution estimated over the meaningful elementary units inside the breast and the scale parameter value. Therefore it is necessary to cutoff all the external elementary squares by taking into account their position with respect to the border of the breast.

Successively, the values of the features computed on the remaining (internal) squares have been normalized to zero mean and unit variance in order to be consistently combined in the computation of the matrix elements 1.16 (cf. e.g. [32]) . A Karhunen-Loève transformation has been subsequently used for reducing the analysis of data to the main independent components of the feature vector and for eliminating eventual feature redundancies.

After computing the mutual distances in the feature space, the K nearest neighbors and the distance scale, the initialization phase concludes by assigning a random value between -1 and 1 for the maps associated to internal points.

The **evolution of the chaotic maps system** is performed only for the effective maps (corresponding to points inside the breast) according to the equation 1.17 where the sum-

mation over couples of maps is limited to the points up to a $3 \cdot a$ distance in the feature space. The number of time steps is fixed since the maps are chaotic. At each step, for each map the sign bit 1.19 corresponding to its current value is extracted and stored as part of a sequence.

Once the evolution of the maps system comes to its end, the **analysis phase** is performed on the sequences of bits according to the procedure described in the equations (1.20)-(1.22). Following the clustering prescription from 1.2.3, the threshold θ is given a series of values in the range $[0, \ln 2]$ and for each of these values the clusters are constructed. Out of the numerical information concerning the total number of cluster and the number of points belonging to each of them, the implementation of the algorithm outputs a "clustered" image on which the clusters obtained on this basis are visualized as different gray-level regions. A number of clusters superior to 256 has been considered meaningless and has been not considered in the analysis. Due to the border effects, the contour of the breast usually introduces a series of spurious clusters with no real meaning. In our analysis, we have chosen to cut-off these artifacts by default assigning a strip of border pixel squares to the unique border cluster; the choice has the advantage that the breast shape contour is immediately visible on the segmented image (in white).

The exposed algorithm implementation can be summarized by the simplified flowchart in Fig. 2.2.

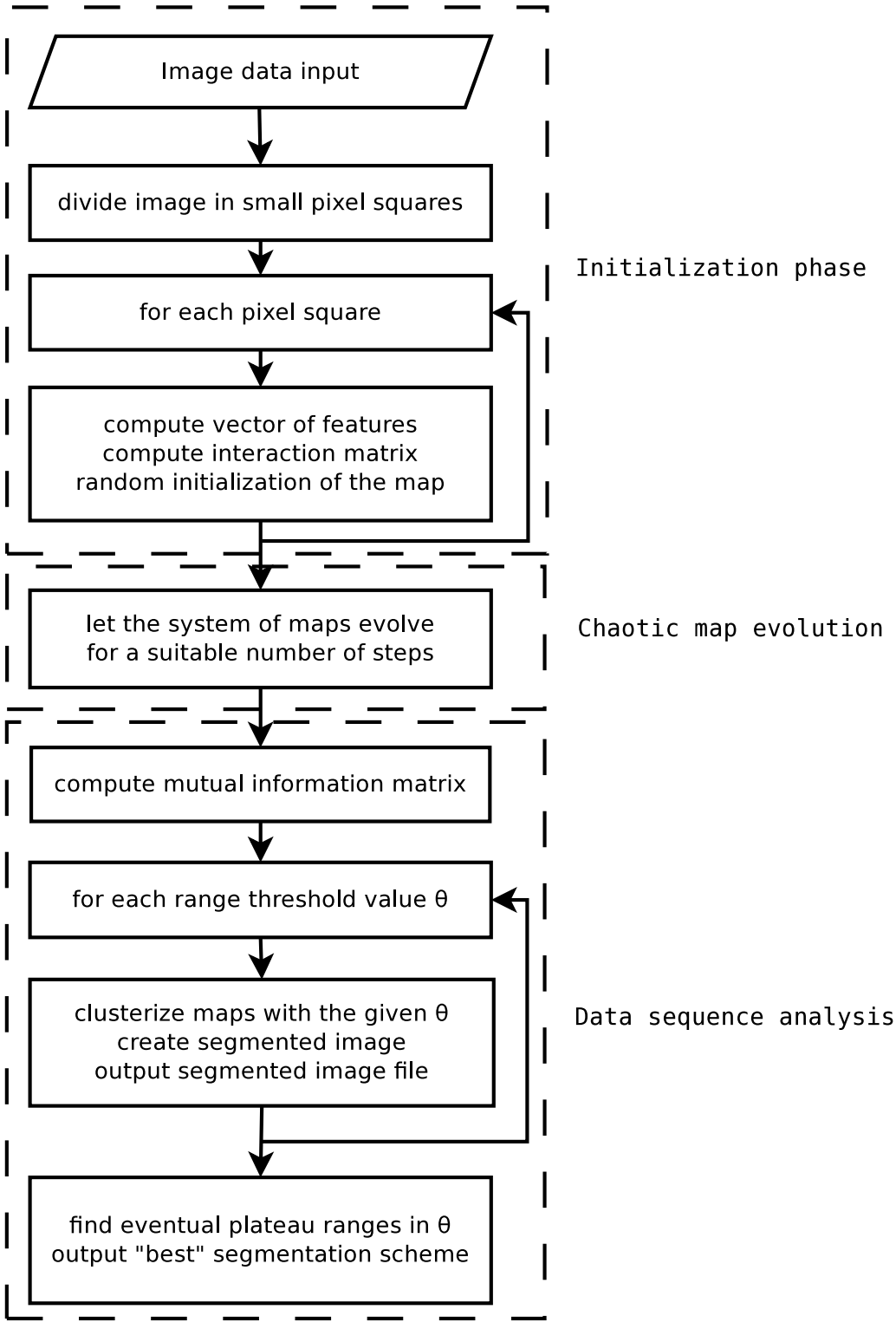

Figure 2.2: Flowchart of the CMC algorithm implementation for segmentation of mammographic images

2.3 Mammographic images segmentation with CMC: results

2.3.1 Results

The application of this clustering method yielded a series of noteworthy results.

There is little to be commented on the evolution of the maps itself: it has been verified that they obey a chaotic dynamics as expected.

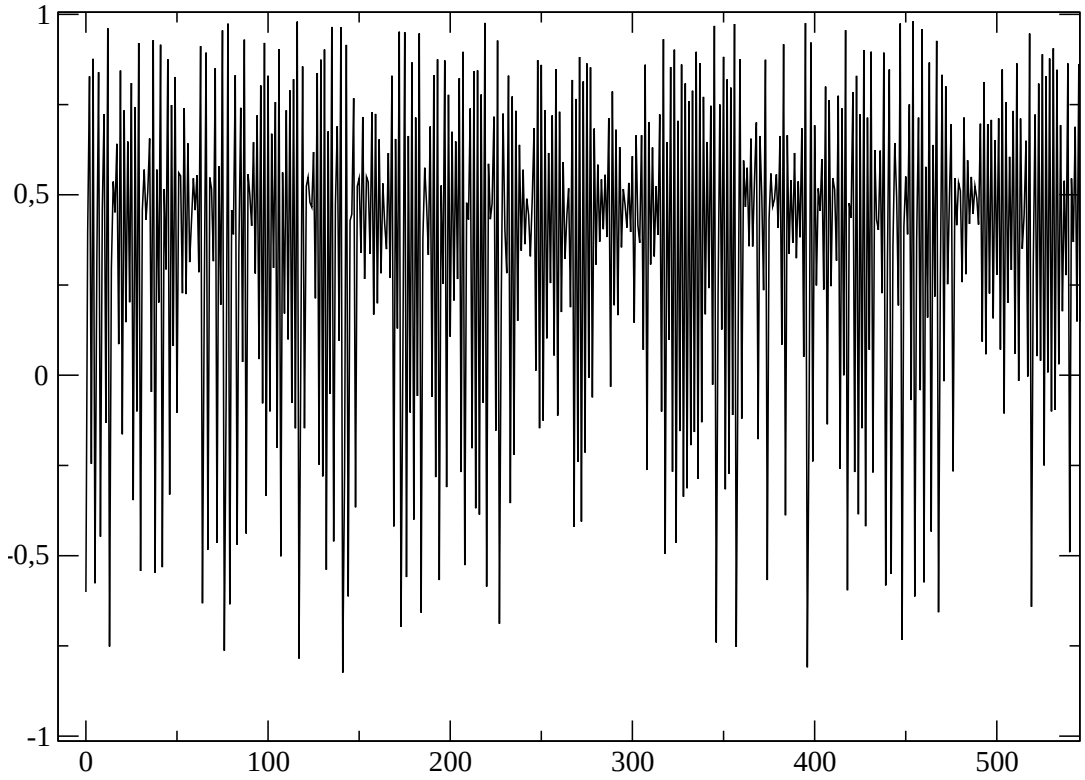

Figure 2.3: Typical dynamics of a map within this implementation

The first important consideration is that for a significant range of values of the defining parameter K (from the KNN) there appears no automatic "best clustering" first criterion

since the number of clusters exhibits no obvious stationarity at the varying of θ. In the runs, values of K ranging from 5 to 50 have been tested, yielding to qualitatively similar results. The typical dependence of the number of clusters as a function of the threshold θ is depicted in the figure 2.4.

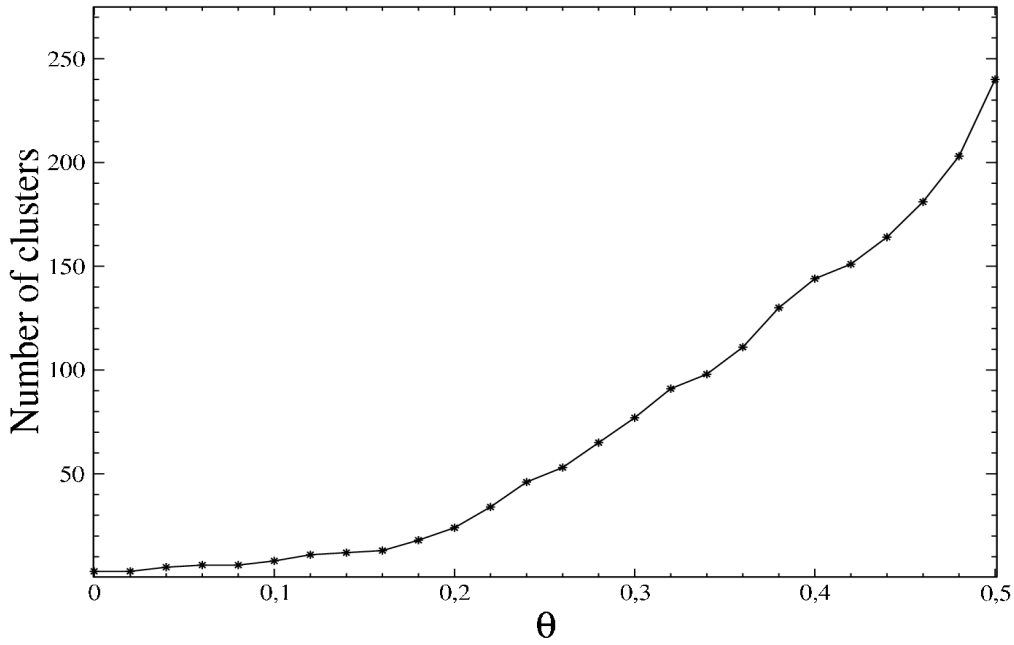

Figure 2.4: Typical variation of the number of clusters as a function of θ

This behavior is not sensibly influenced by the number of features involved in the analysis. As an immediate consequence, the variational approach cannot be mechanically applied just as in the original version of the CMC algorithm.

On another hand, the other evaluation criterion, the size of the biggest clusters, exhibits portions of relative stability at the varying of θ. In order to extract a meaningful behavior, the image partition has to be carefully considered. The final segmented mammogram contains at least the three obvious big clusters:

- the points corresponding to the black background and which lie outside the breast;
- the points assigned to the breast border who are conventionally represented as white;

- the internal points of the breast with no other particularity for the analysis and which naturally group together in an inside background cluster.

When examining the dependence in θ of the big clusters in an image, the three basic clusters have been left out of the analysis since they bear no pertinent information. The typical behavior of the size of the two bigger meaningful clusters is represented in Fig. 2.5.

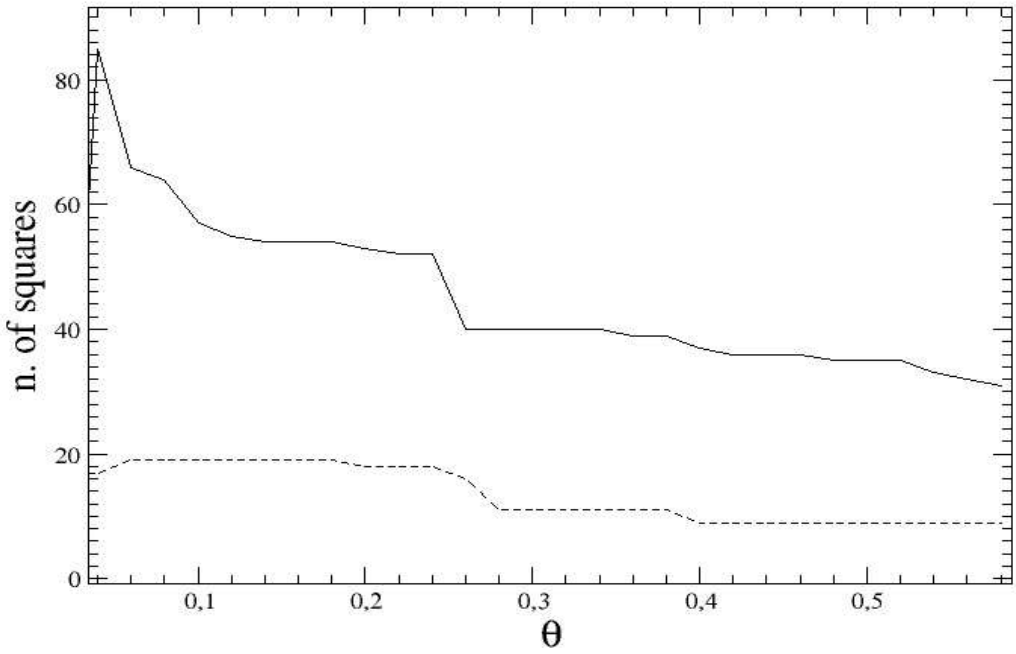

Figure 2.5: Usual variation of the size of the biggest meaningful number of clusters as a function of the threshold θ, the solid line refers to the first cluster, the dashed line to the second one

While most of the meaningful big clusters have significant θ ranges of size stability, about 20% of the images don't present obvious size stability ranges in θ. This fact can be taken as an indication that the obtained clusters in these cases are algorithm artifacts with no medical meaning (an understandable result particularly for healthy patients where the segmentation process is expected to fail to identify potential meaningful regions of

interest, and spurious small clusters are more likely to appear). For the other images, size stability indicates that the big clusters provided by the algorithm do reflect some local property of the image rather than being artificial results of the algorithm.

The lack of stability can be linked with the "cluster noise" which turns out to be very important at higher threshold levels: in fact, most of the clusters contain actually just one pixel square and show up in internal breast areas characterized by rapid variation of luminosity, mostly not far from the breast contour.

The segmentation algorithm described above displays a fair amount of findings in the images containing **mass lesions**. Here are illustrated the most common ways in which the findings of the segmentation algorithm appear.

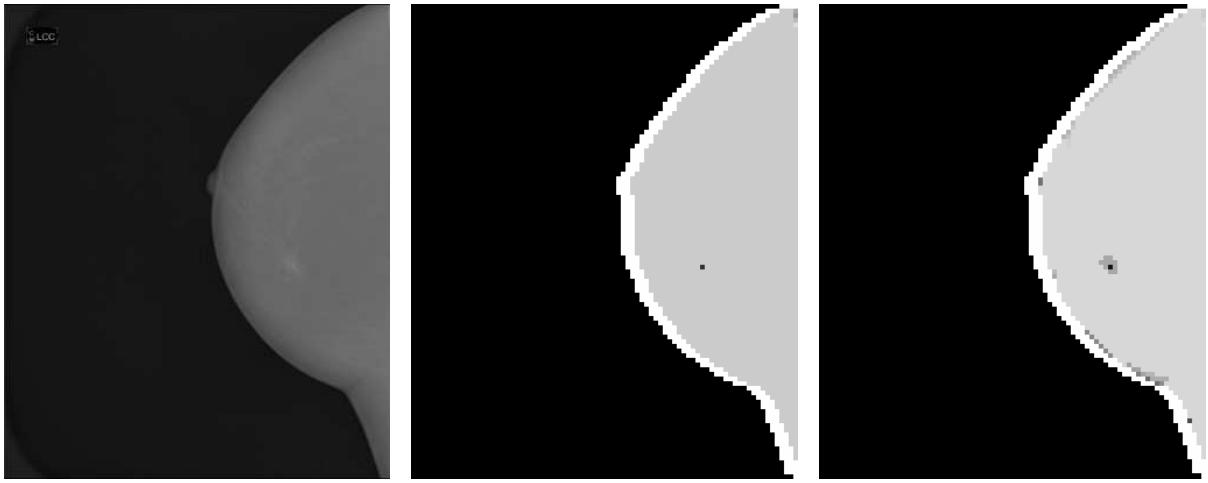

a) Original image b) Segmented image $\theta = 0.04$ c) Segmented image $\theta = 0.36$

Figure 2.6: A small and well-individuated mass showing up in the segmented images

In Fig. 2.6 the segmentation of a small mass easily identifiable on the slightly darker parenchymal tissue is presented for two different values of the threshold. The center of the mass lesion is segmented as unique point cluster for both thresholds. When allowed to search for more clusters (a setting which corresponds roughly to higher sensitivities), a new cluster develops around the center of the mass fairly reproducing its shape, but

with a subsequent apparition of spurious clusters near the border. At lower thresholds, most of the spurious clusters disappear but the shape and size of the lesion are no longer reproduced.

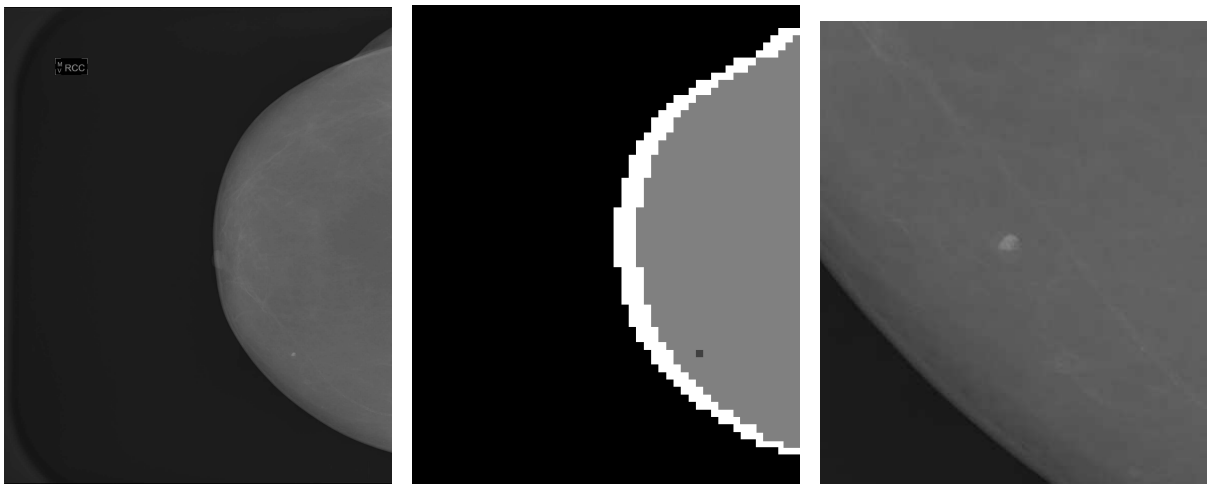

a) Original image b) Segmented image $\theta > 0.02$ c) Enlarged image from a)

Figure 2.7: A small and round-shaped opacity showing up in the segmented images

Figure 2.7 exhibits a basic segmentation pattern showing up at most of the threshold values in the case of a small and well-defined round opacity. In this case, the size of the dense area corresponds roughly to the side of the elementary square and the unique internal cluster showing up constitutes a fine segmentation pattern.

When the potential mass lesions have bigger sizes or they are less contrasted with respect to the surrounding breast tissues, the segmentation process yields less satisfactory results. Two such segmentation patterns are shown in the figures 2.8 and 2.9: the first illustrates the occurrence of a potential mass lesion loss within the process, while the second emphasizes the lack of correspondence between the segmented clusters and the shape and size of the actual opacity in the image.

a) Original image b) Segmented image $\theta = 0.04$ c) Segmented image $\theta = 0.36$

Figure 2.8: Medium-sized massive objects in a mammography segmented with $\theta = 0.04$ and $\theta = 0.36$. Note the spurious pixel squares near the upper cluster and the lonely pixel square cluster showing up at higher θ

The mass loss in the segmentation phase occurs frequently for larger mammogram dense areas. While for the small opacities the clusters essentially match the area of interest, the algorithm frequently assigns elementary units belonging to the larger ROI to different clusters, easily confoundable with spurious findings. The scarcity of valuable results in the case of the potential mass lesions makes impossible to estimate any reliable quantitative performance parameter e.g. in terms of true positives, sensitivity or ROC curve: it is very difficult to decide whether a generic mass has been identified by the segmentation process and there is a cluster of points reproducing it up to some extent.

An interesting behavior is displayed by the images containing **micro-calcifications**. The parts of the image where micro-calcifications show up naturally group altogether in a cluster. The feature analysis thus displays the whole ROI rather than finding individual calcifications, as is visible in the Figure 2.10. This result it is also not surprising due to the well-known reliability of the micro-calcifications characterization through the local

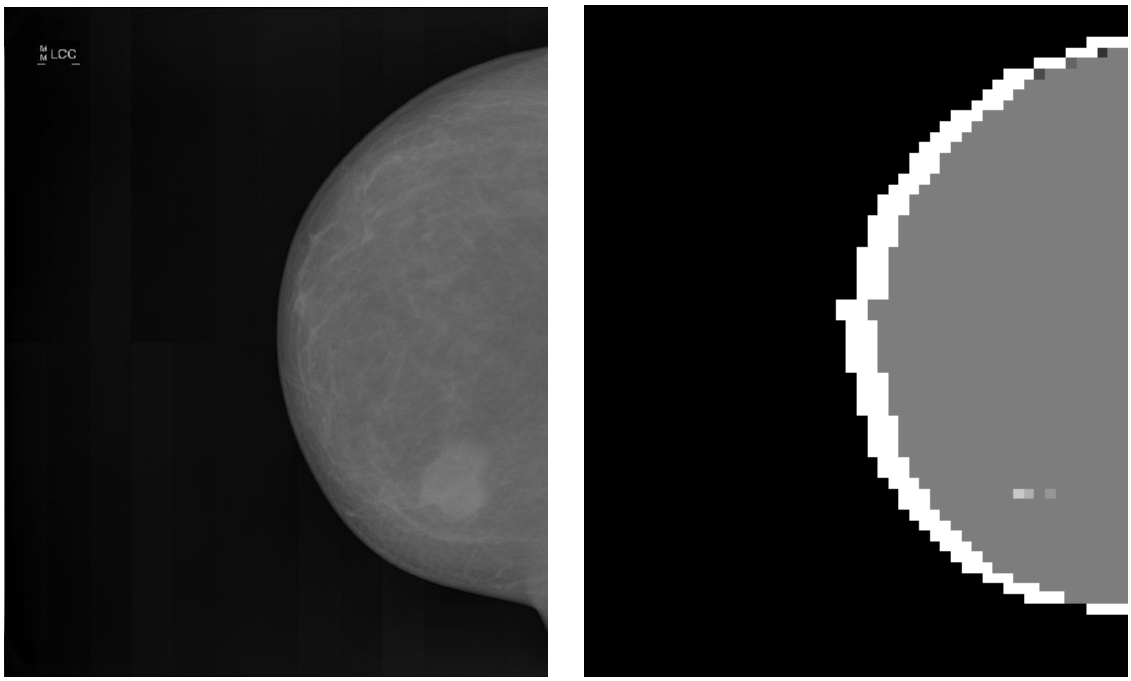

a) Original image b) Segmented image $\theta = 0.10$

Figure 2.9: Large-sized density object in a mammogram segmented with $\theta = 0.10$. Note the weak correspondence between the segmented internal areas and the actual shape and size of the ROI

features on the image.

Since the segmented image looks promising for an eventual further analysis in an automatic system, a validation alternative approach has been used: instead of clustering mutual information for the bit sequences, the simple Euclidean distance in the feature space between the couples of squares has been considered as dissimilarity parameter. With this data available, the clustering has been performed in a similar manner to the one exposed in 1.2.3: all the couples of points separated by an Euclidean distance inferior to a given threshold have been graph-connected, while remote points remained disconnected. The connected parts of the graphs provide the partitional scheme; the reliable feature-based partition of the image in figure 2.10:a is shown in 2.10:d.

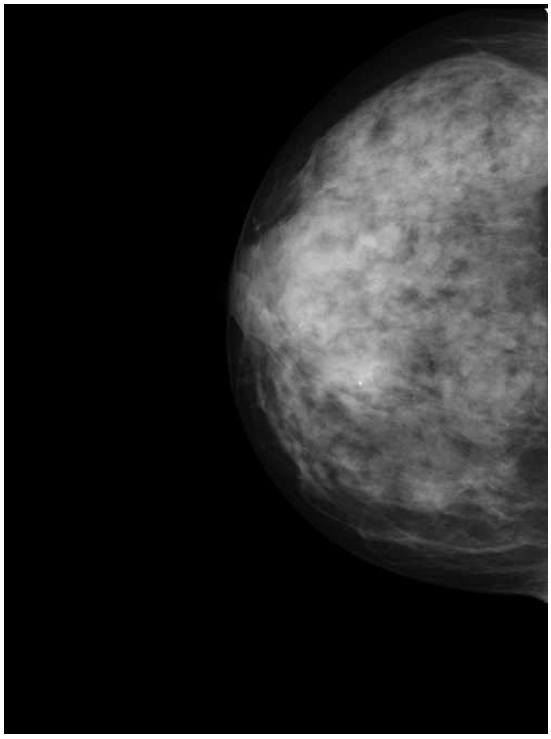

a) Original image containing micro-calcifications clusters

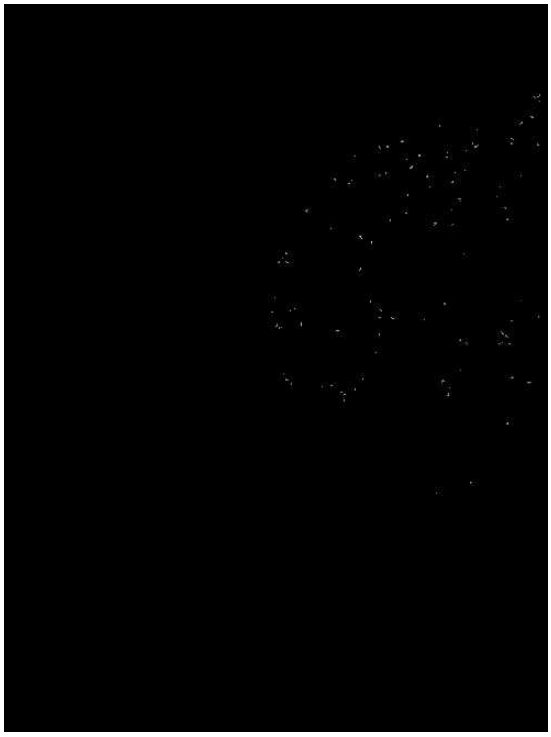

b) Micro-calcifications distribution given by a CAD tool

c) Segmented image displaying a big cluster for the ROI

d) Image segmented with a feature-based dissimilarity scheme

Figure 2.10: Segmentation of an image with micro-calcifications

As one can easily notice, the feature-only based approach produces a segmentation pattern essentially similar to the one given by the CMC method here examined. Therefore, the chaotic map clustering of the mammographic images containing micro-calcifications brings out no extra information with respect to this simpler and less resource consuming method. An immediate interpretation of this fact would be that for the mammograms considered here the clustering properties are not heavy linked with the algorithm itself but rather with the chosen system of features and feature space distribution of representative points.

2.3.2 Discussion

The non-parametric chaotic map clustering of the mammographic images has been considered here as stand-alone segmentation approach, mainly from an application point of view. The ultimate goal of applying such a particular segmentation method to the medical mammographic images is the potential performance improvement of an automatic detection system based on it. As hinted, the specific aspect of mammographic segmentation which still constitutes a non-trivial challenge, is the segmentation of mass lesions, while the identification of micro-calcifications with this new algorithm hardly could lead to any spectacular breakthrough advance. Since there is no clear stability range in the threshold θ , assigning these findings to real ROI for a medic (potential mass lesions) remains a hard task, at least for an automatic system such as a CAD. Basically similar segmented images can be obtained with less effort if clustering only the distance features, which means that the chaotic map clustering algorithm brings little (if any) improvement with respect to the more orthodox and less resource consuming distance-based methods. This result is certainly not surprising since if one excludes their geometrical characteristics, mass lesions usually do not share a mathematically well-defined set of features and the identification of massive ROI is a challenge.

At this stage of the analysis, the results lead us rather to pessimistic conclusions concerning the valuable applicability of the chaotic map algorithm for the segmentation of mammographic images in an efficient automatic work-flow. While some massive opacities show up conveniently as internal clusters (especially the smaller ones) in the segmented images, many of them are either lost or they appear with wrong sizes, shapes and as neighboring independent clusters (see e.g. Fig. 2.8 and 2.9). This fact implies that the massive opacities segmentation with this algorithm does not really meet the basic requirements of the task itself. Moreover, the important number of "parasite" clusters with no medical significance add a further complication in correctly evaluating the output of the segmentation algorithm which the stability analysis cannot eliminate. Concerning the

micro-calcifications, the fairly decent results of the chaotic maps segmentation process are still not better than the ones derived from simple feature analysis. Consequently, there would be little point in using this further elaboration technique which adds nothing to the information already available about the mammographic image. Within this interpretative framework of the results, even with the limited statistics of the cases used in this thesis, we can summarize our analysis by asserting that due to the particularities of the mammographic images, the chaotic map clustering algorithm could hardly prove in the future to be a good valid stand-alone method of segmentation. Whether this method could improve the segmentation performance of another jointly used algorithm or be successfully used in a subsequent analysis stage such as the classification of the segmented ROI should make the object of a further work.

Chapter 3

Indirect Immunofluorescence images classification

3.1 Introduction

3.1.1 Immunofluorescence overview

An autoimmune disorder is a disease occurring when the (human) body's immune system develops an inappropriate immune response against own cells by mistakenly attacking and destroying healthy body tissue. The normal immune response is directed against (potentially or actually) harmful or alien substances and cells and it is chemically triggered by a molecular structure recognizable by the immune system, called *antigen*; a very limited attack against body's own cells is a part of the normality. The aberrant behavior of the immune system consists in erroneous massive "recognition" of body's own cells as harmful and subsequent misdirected autoimmune response. Within this condition, the immune system produces autoantibodies and T-lymphocytes of immunological competence which will heavily act against body tissues producing structural and/or functional damage.

There are more than 80 different types of known autoimmune disorders ([83]), which can be labeled as haemocytolytic (involving blood circulation cells), localized (affecting

a specific organ) and systemic (affecting the whole organism). Taken as a whole, the autoimmune diseases constitute the third most common group of diseases in the United States, second only to cancer and heart diseases, which affect an (under-)estimated 5-8% of the population ([84]).

The relatively high incidence of autoimmune diseases makes necessary the development of effective specific detection systems. Among the clinical tests routinely used in the diagnosis of autoimmune disorders/diseases, a place of choice is occupied by *Immunofluorescence*, which constitutes the standard recognition test in screening programs [93]. First developed by Coons around the mid 20^{th} century ([94], [95]), Immunofluorescence techniques are based on the reaction antigen-antibody in which the antibodies are tagged (marked for visualization) with a fluorescent coloring agent and the complex of both the antigen and the marked antibody is subsequently visualized with a microscope using for illumination ultra-violet light. The dyes regularly used within this technique are called fluorochromes; they have the role of emitting visible light under appropriate ultra-violet incidence.

The immunofluorescence techniques fall in two basic categories:

Direct Immunofluorescence (DIF) This group contains those techniques characterized by the staining of cells with antibodies (AAB) directly bond chemically to the fluorescent dye. The antibody recognizes its specific target molecule and establishes a bond to it; the attached fluorochrome is subsequently detected with the fluorescence microscope after washing out the unbound antibodies and other non-antibody proteins. The use of a DIF technique makes possible multicolour tests, where the cells are simultaneously stained with different species of antibodies, each one marked with a different fluorochrome.

Indirect Immunofluorescence (IIF) These techniques are characterized by the use of two antibodies: the cells are at first stained with unlabeled primary antibodies by

allowing the substrate to react with patient's serum of various dilutions (1:40, 1:80, 1:160 etc.) in a damp chamber for about half an hour, then in a second step, after a rinse the other antibodies of defined specificity labeled with fluorochrome (usually fluorescein isothiocyanate, FITC) are introduced in order to bind with the primary ones. As well as in the case of DIF, the exceeding (mostly fluorescent) antibodies are removed through a final washing before slides examination under the microscope. Although multicolour images can be obtained in special conditions, IIF techniques are basically monochrome.

Of particular importance in the detection of autoimmune diseases are the Antinuclear Antibodies (ANA) whose actions are targeted against a broad spectrum of nuclear antigens and which are identifiable in patients serum. While on the market have appeared immunoenzymatic technique (ELISA) diagnostic kits, the simplicity of this potentially automatized method is partially shadowed by its inferior sensitivity and reliability with respect to the standard recommended IIF ANA test [87], [88]. The use of a human epithelial cells line (HEp-2) as antigenic source for ANA tests makes possible the detection of a large number of autoantibodies species; on another hand, the HEp-2 line substrate exhibits a good sensitivity for determination of ANA [89].

Although the IIF remains the preferred AAB determination method, it has also a certain number of limitations and drawbacks such as the non-uniformity of the substrate, the non-automatic manipulation of the samples or the subjective interpretation of the results which lead to a low reproducibility and an overall lack of standardization [98]. Moreover, IIF assay is noteworthy for the impossibility of its automation and being thus time-consuming, with all additional costs implied [99]. A partial answer to these limitations could be the application of automated interpretation systems in IIF, a method which could eventually bring higher standardization for the technique [96], [97].

Henceforth, the present analysis will concentrate exclusively on IIF tests performed for

ANA on the HEp-2 substrate.

3.1.2 IIF images classification

The IIF tests performed on HEp-2 substrate using FITC fluorochrome produce green band images ($\lambda_e = 518nm$) which are usually digitized by color cameras. While the visual information is recorded on a three-channel color system, the only meaningful input obviously reduces to the monochrome green emission band of FITC which carries all the information about the relevant antibody fixation on the substrate cells, and is reproduced essentially losslessly by the green channel of the digitized image [102].

The analysis of an IIF image can be divided in three main hierarchical processing steps [96]:

1. positivity of the image (if the patient serum contains a medically significant amount of ANA), usually realized in function of the fluorescence intensity;

2. localization of the fluorescent pattern(s) – nucleus, cytoplasm, mitotic cells chromatin;

3. nuclear pattern characterization.

Other authors combine the steps 2 and 3 in a generic staining pattern classification phase ([102]).

The **fluorescence intensity** classification step discriminates between healthy patient negative images and positive images indicating the presence of ANA in patients sera. The physician recommended classification makes reference to a semi-quantitative scoring for the characterization of the positive images according to their fluorescence intensity [103].

Score	Fluorescence intensity description/characterization
4+	brilliant green (maximal fluorescence)
3+	less brilliant green fluorescence
2+	defined pattern but diminished fluorescence
1+	very subdued fluorescence
0	negative

The guidelines [103] proposed by the Centers for Diseases Control (Atlanta, USA) include the use of two standard "controls", positive and negative, to which the analyzed image has to be compared. The *negative control* is a specificity test for the involved antibody: if the serum to be tested is normal (healthy) no staining intensity should show up. The *positive control* is obtained by using known positive serum for the test and constitutes basically a procedure validation test. Both control tests are used as a comparison check by the physician and they are important in defining a particular calibration for any automated image analysis technique.

It's worth mentioning that recently, a new classification of sample fluorescence intensity has been proposed [104]: according to its authors, the first classification step should label IIF images as *negative*, *intermediate* or *positive*. The classification relies on a double-reading expertise. The proposed three-class system results by the mapping of the combined class assignments by two independent physicians:

- an image is *positive* if both physicians label it at least as 2+
- an image is *negative* if both physicians classify it as negative
- an image is *intermediate* or *border zone* if both physicians classify it as 1+ or if their labels disagree and at least one of these labels is inferior to 2+.

This three valued classification system is also used and discussed in the present work.

The **staining pattern classification** step is aimed to assign the cells images to one or more among the more than 30 different patterns described in the literature [99]. This assignment reveals an information potentially useful for diagnostic purposes, since different patterns correspond to different sets of autoimmune diseases. Although the number of patterns seems excessively high, not all of them are frequently encountered in practice; most often, the nuclear staining patterns will fall in one of the following groups (e.g. [90]):

- Homogeneous (Diffuse): staining of the interphase nuclei and staining of the chromatin of mitotic cells
- Nucleolar: homogeneous or large coarse speckled staining of nucleoli within the nucleus
- Speckled: (fine to coarse) granular nuclear staining of the interphase cell nuclei
- Peripheral nuclear (Rim): continuous staining around the outer region of the nucleus, with definitely weaker staining toward the center of the nucleus
- Nuclear dot: 2 to 30 (commonly 13 to 25) dots in interphase nucleus
- Centromere: more than 30 nuclear dots in interphase nucleus and mitotic cells chromatin

The CDC standardization [103] recommends the use in reports of the first four (nuclear) patterns from above, along with the cytoplasmic staining pattern characterization. In order to complete the overall picture, one has to add that in a significant number of cases two (or more) staining patterns are present in the image which should be labeled as *mixed*. In an automatic work flow for the analysis of IIF images, the two classification steps are to be performed in sequence, the staining pattern label concerning exclusively those images categorized as positive at the first step. Both of them can be in principle realized through application of the CMC algorithm. While the fluorescence intensity classification has been successfully performed on the basis of a whole image system of features ([106], [105]), the

nuclear staining pattern assignment has to be performed on every single cell of the image, which requires a certain preliminary image processing. Therefore, the pre-classification of the IIF images with a new algorithm can be implemented easier and faster than the classification of the single cells after developing also a specific preprocessing tool, and require a more complex analysis. It's worthwhile mentioning that the segmentation from the preprocessing phase in the case of the IIF images is easily performed by standard methods such as thresholding, so it would be pointless to use the more complex CMC approach in order to generate a segmentation of the image (here, this step of the analysis is not critical!).

Although in the literature are mentioned various automated systems of classification of IIF images, only a part of them contain an explicit positivity pre-classification module and among these latter ones, only the multiple expert system proposed by Soda and Iannello ([107], [106]) is properly described in details, while noteworthy performance of the commercial AKLIDES system is repeatedly mentioned without further specifications ([97], [96], [101]). The approach used here exploits the worthy aspects of the multi-expert system made available in the literature.

3.2 Materials and methods

3.2.1 IIF images

Usually, the IIF images come in groups of several dozens of different patient samples (positive or negative) along with two calibration images: the negative and the positive controls. As previously indicated, all IIF images used here have been obtained on the HEp-2 substrate of epithelial cell lines obtained from human laryngeal carcinoma, a choice leading to good visualization of the internal structure of the cells from an homogeneous population of monolayer individuals.

While routine laboratory ANA tests are performed starting with the recommended initial sample dilution 1:40 which is subsequently decreased by halving it until its titer corresponds to the disappearance of the fluorescence signal, the IIF images considered in this thesis are all made at the threshold dilution of 1:80. From the medical point of view, this choice is justified by the low positivity titer range which is (1:40 – 1:160) for most laboratory tests (that is: dilutions lower than 1:160 are to be considered definitely positive, while concentrations higher or equal to 1:40 correspond to negative sera, the intermediate values being labeled as low positive) [106]. The choice is also justified by analysis uniformity which requires to compare sample images taken in similar conditions.

The reduced IIF image database used for this work contains a total of 90 sample images pertaining to 6 different slide determinations (each slide having one couple of corresponding controls). All the images have been reviewed and classified by one or two expert immunologists as true positives (66), border zone (3) and true negatives (21). The 66 positive images exhibit the following staining patterns:

- 25 Speckled
- 18 Homogeneous
- 7 Nucleolar

- 2 Centromere

- 14 mixed patterns (3 Homogeneous + Nucleolar, 3 Speckled + Nucleolar, 3 Speckled + Mitosis, 1 Speckled + Nuclear Dots, 1 Speckled + Cytoplasmic, 1 Speckled + Mitochondrial, 1 Homogeneous + Nuclear lamina, 1 Nucleolar + Peroxisomes)

As easily seen from the exposed structure, while fairly reflecting the routine distribution of the samples in a laboratory IIF analysis, the statistics of this database are far from being highly relevant with respect to the fluorescence intensity pre-classification (the border zone case is practically absent) and of limited interest in which concerns any investigation about the staining pattern classification (only speckled, homogeneous and – in a lesser measure – nucleolar patterns can be described with partial relevance). Two samples of the most relevant staining patterns are displayed in figure 3.1.

The image files have the three standard color channels at the same camera resolution of 650×515 pixel; they have been reduced to their monochrome intensity levels which are essentially coincident with the green channel value (since the intensity levels for the red and blue channels are practically zero with some meaningless noise added). Therefore, each image is fully characterized by its 334750 pixel intensity levels which constitute the input to the present implementation of the CMC algorithm.

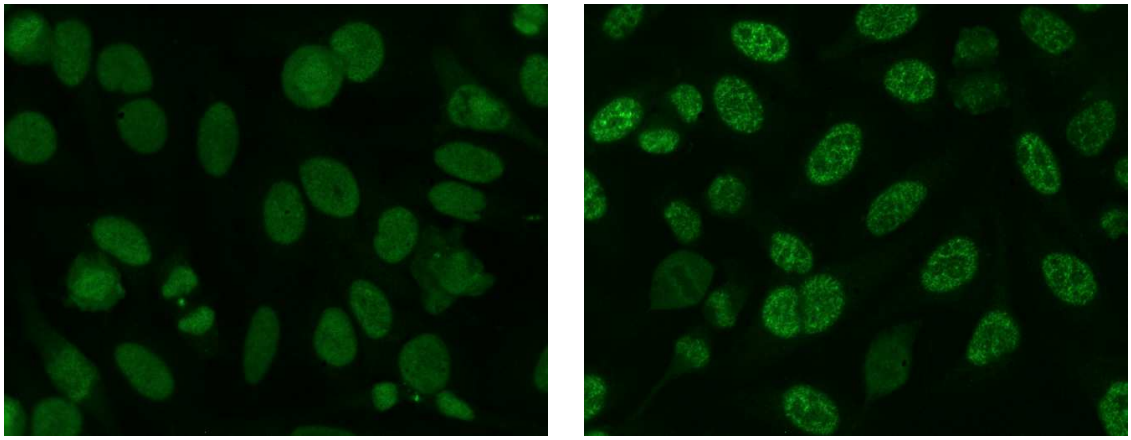

a) Homogeneous pattern b) Speckled pattern

Figure 3.1: Samples of the most frequent nuclear staining patterns in the database

3.2.2 Specificities of CMC algorithm implementation

The characterization of an image must be done in terms of a carefully chosen set of features. It has been argued and tested ([106]) that the whole image features informational content is matched by the information corresponding to the features computed exclusively on its cell area (after segmentation):

- the practically uniform dark background of the IIF images contributes scarcely to the statistical features;
- the pertinent features are correlated to the essentially similar texture pattern of the image cells;
- potentially harmful artifacts introduced by the segmentation algorithm don't show up within this set up.

The CMC algorithm works well on appropriately normalized features in the data space. One has to take into account that physicians themselves compare the IIF image with the positive and negative controls in order to assign a label for its fluorescence intensity. The approach used in [106] considers that each absolute feature of the analyzed image comes

along with *four* other values which can be seen as different features; if one denotes by f_{im}, f_{CP} and f_{CN} the numerical values taken by a feature computed on the processed image, on the positive control image and on the negative control image respectively, the four combined features take the values $f_{im} - f_{CP}$, f_{im}/f_{CP}, $f_{im} - f_{CN}$, and f_{im}/f_{CN}. While these values suit the multi-expert decisional system used in the above cited work, the purposes of a CMC-based classification system are fit rather by the naturally scaled (reduced) features:

$$f_{red} = \frac{f_{im} - f_{CN}}{f_{CP} - f_{CN}} \tag{3.1}$$

The system of features used for the overall characterization of the IIF images in the database contained the following groups of elements [1]:

first-order histogram: first 4 moments of the distribution, entropy, range

second-order histogram: second-order entropy, contrast, angular second moment, inverse difference moment, correlation, marginal means, marginal deviations, entropy of difference second-order histogram, difference second-order histogram angular moment, difference second-order histogram mean

distributional: position of absolute maximum, energy around the maximum, number of relative maxima, energy around relative maxima

A preliminary analysis of the system of features reveals that not all of them have effective discriminant power. In order to have a seizable representation of the separation capabilities of the reduced features mentioned above, an "as is" statistics has been performed on the IFI images from the database. On the graphic in Fig. 3.2 the averages and the standard deviation bars on the whole database and on its three subsets have been represented. As the visual inspection clearly shows up, only a limited group of features have potentialities of discriminating positive and negative images, while the border zone images (already coming into play with very poor statistics) meet serious difficulties to

[1] The computation of these features is detailed in the Appendix B

be separated from the rest of the images (particularly from negative images) exclusively through feature-based methods. More specifically, the features with distributions enabling

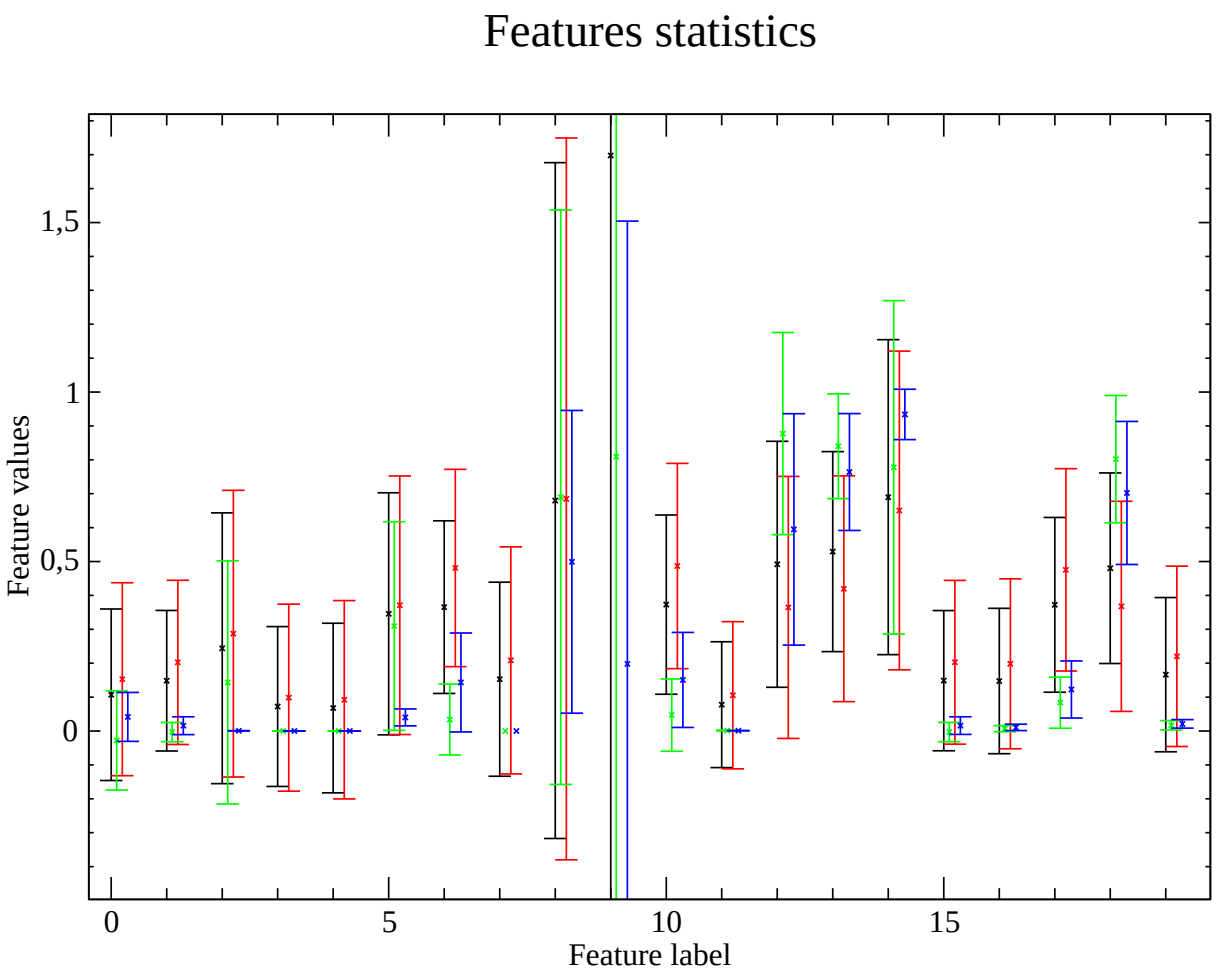

Figure 3.2: Features statistics: average values with standard deviation bars. The black marks refer to overall database values, the red color stands for positive images, the green color is associated to negative images, while the blue marks are for the border zone images. The features are scaled according to the relation (3.1) but not normalized

them to separate between positive and negative images are the non-overlapping ones (6 – first-order entropy, 10 – second-order entropy, 17 – entropy of difference second-order histogram, see Fig. 3.3) and, to a lesser extent, other lightly overlapping with favorable distributions (1 – the histogram average, 12 – the angular second moment, 13 – second-order inverse difference moment, 18 – differential second-order histogram angular moment,

Fig. 3.4). Unfortunately, the three non-overlapping features, all of them being entropies of some kind, are actually highly correlated (see fig. 3.5), which means that only one of them is a really pertinent discriminant characteristic).

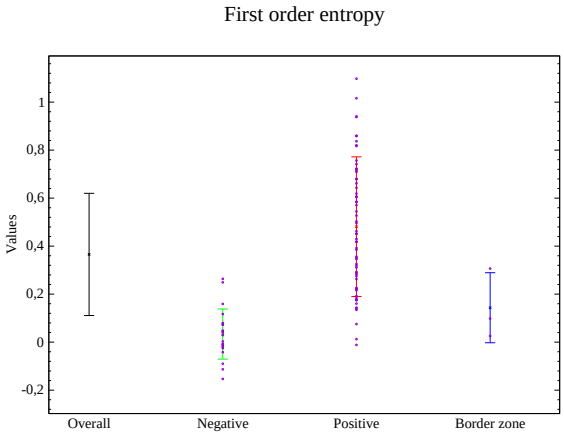

a) First order entropy

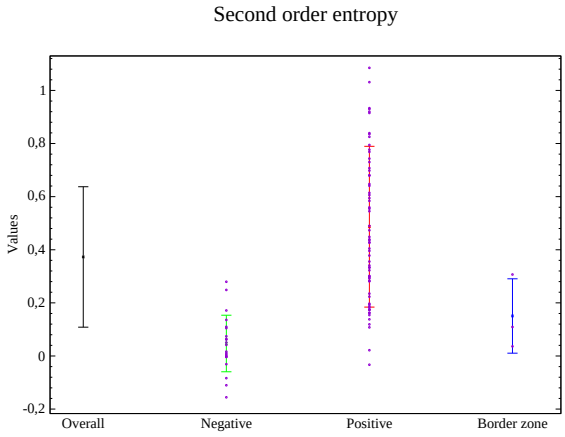

b) Second order entropy

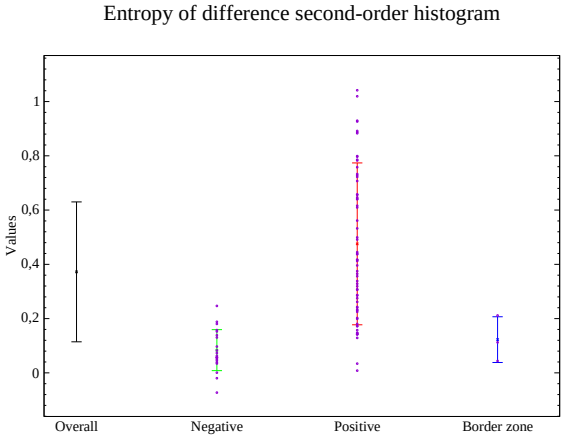

c) Entropy of difference second-order histogram

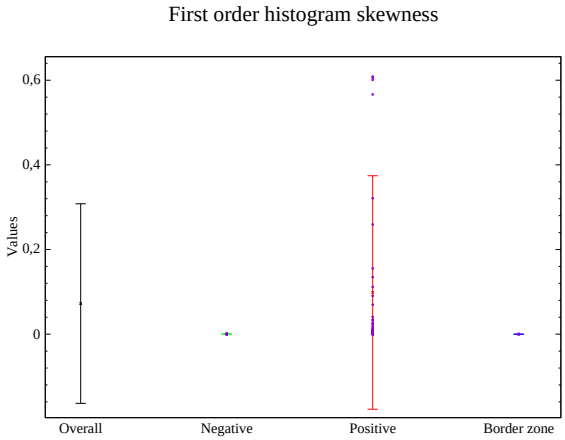

d) First order histogram skewness

Figure 3.3: Detailed distributions of top-discriminating features to be compared with a non-discriminating feature (d). The representative points of the images are figured as small circles

The effective implementation of the classification algorithm has to take into account these considerations. The data type suggests the use of a *decomposition method* (i.e. the

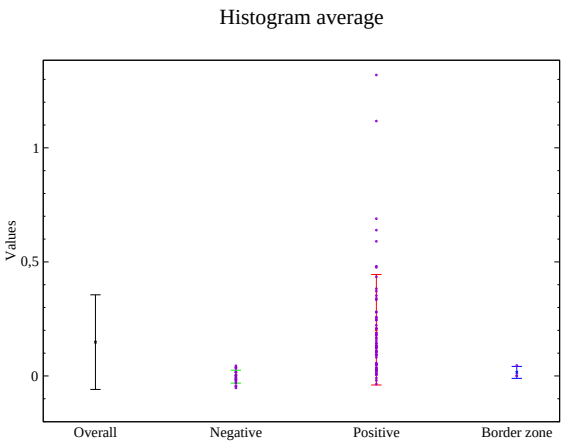

a) Histogram average

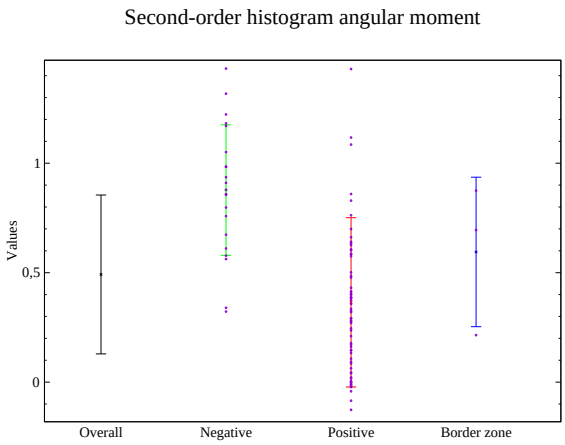

b) Angular second moment

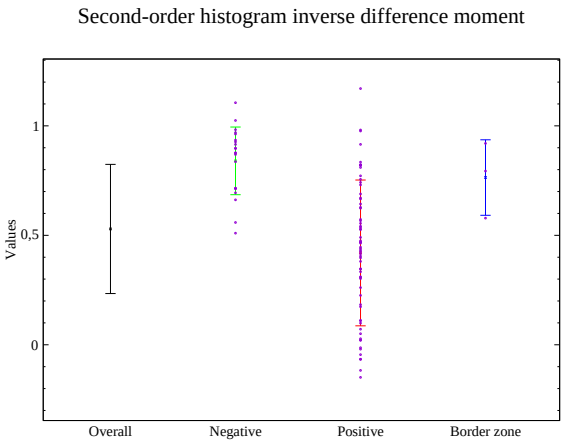

c) Second-order inverse difference moment

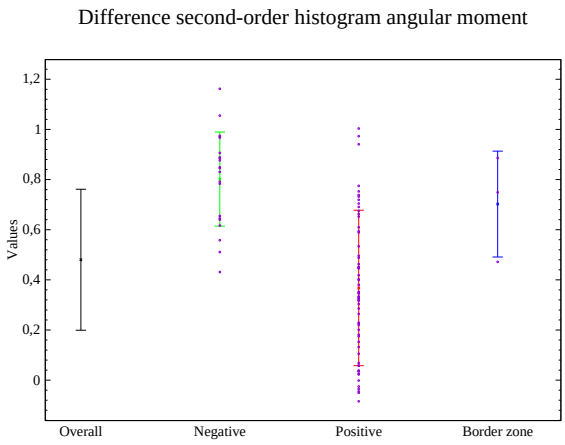

d) Difference second-order angular moment

Figure 3.4: Detailed distributions of the four marginally discriminating features

reduction of the multiple class categorization issue into several binary tasks) rather than a *direct multiclass* approach ([108], [109]). Let aside the *pairwise coupling*, the *distributed output code* and the n^2 *classifier*, the method chosen to better cope with this kind of data is a modified *one-per-class*. Within this approach, a decisional module makes the distinction between one group members and the "rest of the world". The definitive classification of an element comes by combining the decisional outputs of the modules with an appropriately chosen *reconstruction method*. Each of the decisional modules involved makes use of the CMC algorithm for determining the final assignation of an image; unlike

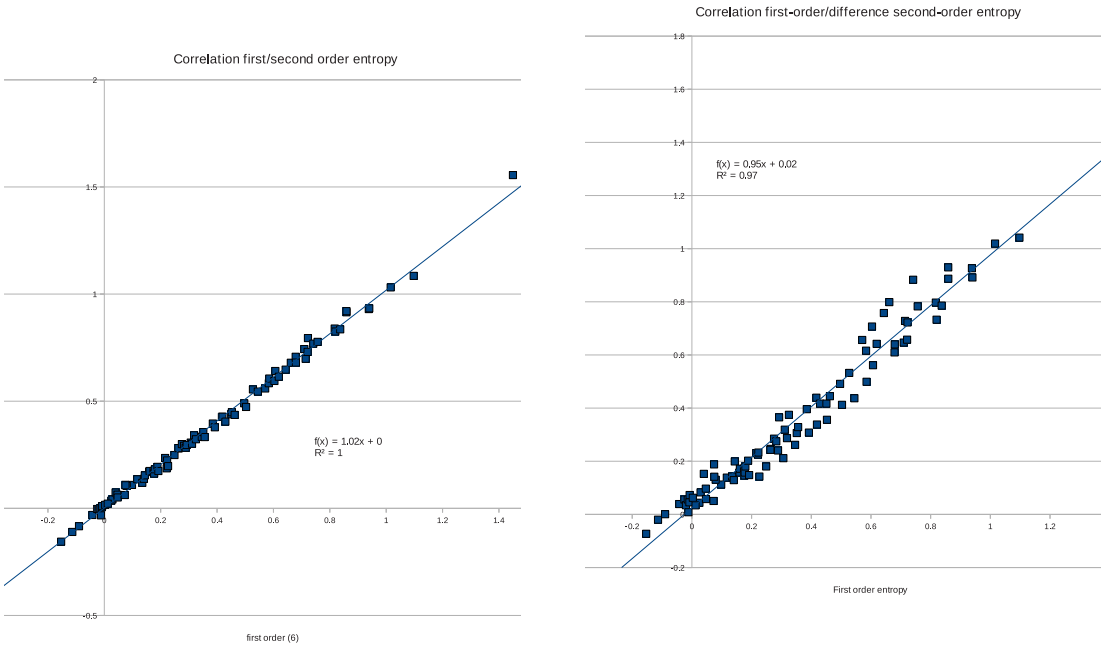

a) First vs. second order entropies

b) First vs. differential second-order entropies

Figure 3.5: Linear correlation of the three discriminant entropy features

in the case of segmentation, here the final number of clusters is known and the threshold parameter has to be chosen accordingly in order that the final classes optimally match the algorithm output. The slightly modified flowchart of the CMC algorithm in the strict sense is presented in Fig. 3.6. The input image class is given by the majority rule applied in the final cluster containing it: if most representative points in the considered partition correspond to a given class A, the input image should be assigned to the same class A. The two obvious modules which have to be used in the present case are a positive and a negative discriminant. With a definitely better statistics, one could probably add a third discriminant module corresponding to the border zone images. Each module uses a different system of features which better suit its classification necessities. Within this configuration, the final output label of an image is set to be definitely positive or negative

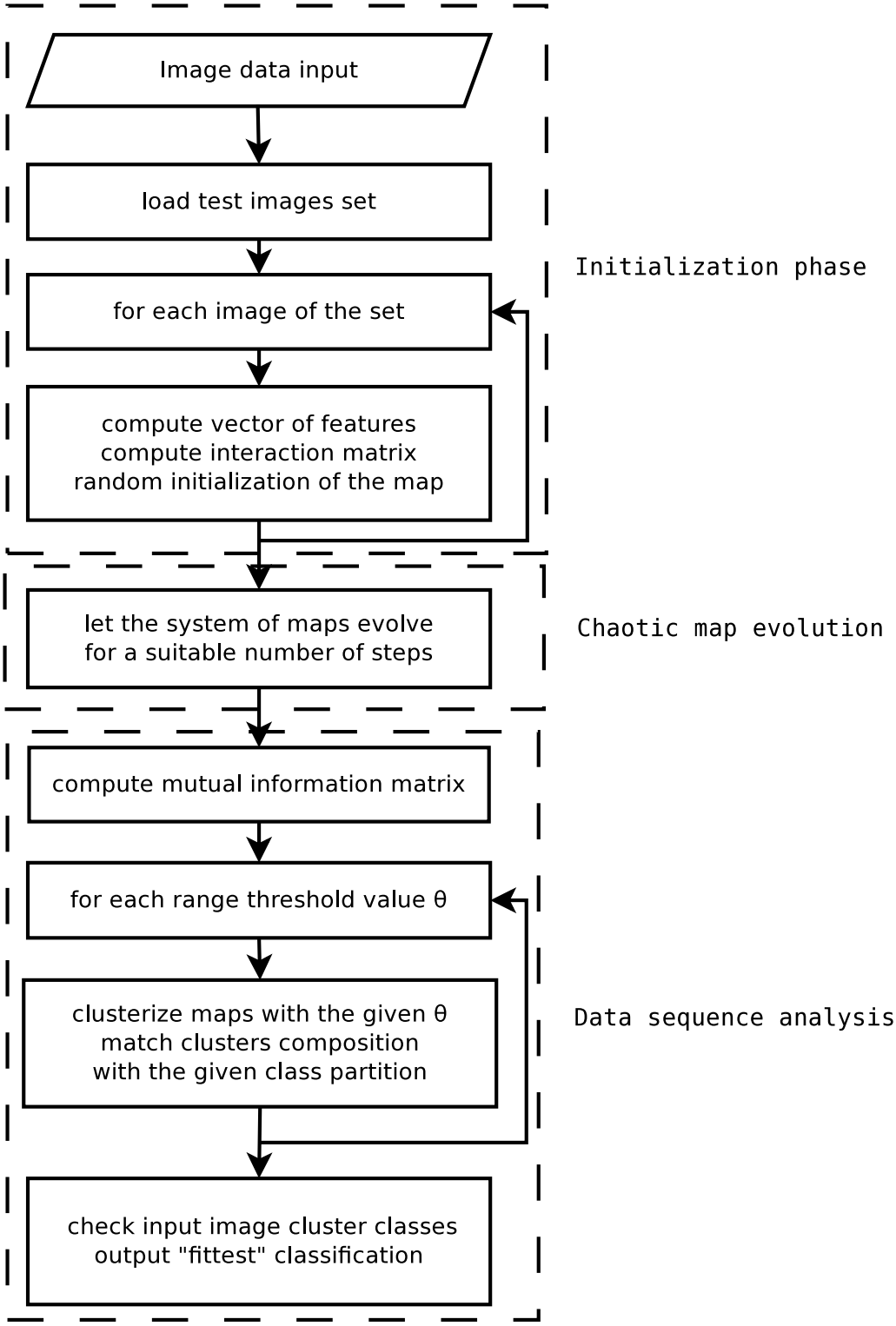

Figure 3.6: Flowchart of the CMC algorithm implementation for classification of IIF images

if both modules agree (that is: the positivity module classifies the image as positive and the negative module classifies it as non-negative, or the positivity module classifies the image as non-positive and the negative module classifies it as negative), while the image is considered border zone in case of disagreement (i.e. both modules claim image membership for their group or they both dismiss it). The attribution scheme is schematized in the table 3.1.

		Positive module class	
		Positive	*Non-Positive*
Negative module class	*Negative*	Border Zone	Negative
	Non-Negative	Positive	Border Zone

Table 3.1: Multiple-Module output scheme (colored words)

Since the IIF image pre-classification phase has to give ultimately an answer to the question of processing or not the analyzed image, the utility of the third choice (border zone) at this point of the whole process is actually very limited. The rational output of this phase should be simply binary, as required by its integration in the normal flowchart of an automatic complete classification system, and it should exclude from further processing the definitely negative images, while the positive (or rather: non-negative) images should undergo a deeper investigation. Within this context, the three-folded classification seems to bear just some residual relevance for the physician, a border zone image corresponding to a case to be followed up.

An extended referenced IIF database appears to be a natural application field of the CMC algorithm whose primary power is the discriminating power between several different classes. In this case, the algorithm should differentiate and classify the cell staining patterns.

3.3 IIF images classification with CMC: results

3.3.1 Results

The application of the CMC algorithm in the classification of IIF images lead to interesting results, despite the inherent limitations of the database. Each image has been represented through the system of reduced features 3.1 as a point in the feature space. It's worth emphasize here some results of the analysis phase:

- with two exceptions (energies around maxima – features 8 and 9) the reduced features have comparable variation ranges, being thus acceptable for a further processing with the CMC algorithm, even without normalization;
- the variation range of the positive sample IIF images is essentially wider than the ranges of the negative and barely relevant border zone samples: this is expected due to the high diversity of the positive IIF images with respect to the low luminosity negatives;
- granted that the three border zone images statistics has to be taken "as is", there appears to be little difference (if any) with the negative images with which there is no really discriminant feature;
- while the statistical discriminant power over the negative and border zone images is the most marked, due to their broad feature range, the positive images are expected to get the maximum amount of false identifications: there will always be some badly placed representative points in the feature space.

As mentioned, the classification system used here is composed of only two modules, since a Border zone expert (see e.g. [105] could not be conveniently established. The difference between the modules relies in the choice of the discriminating features to be used.

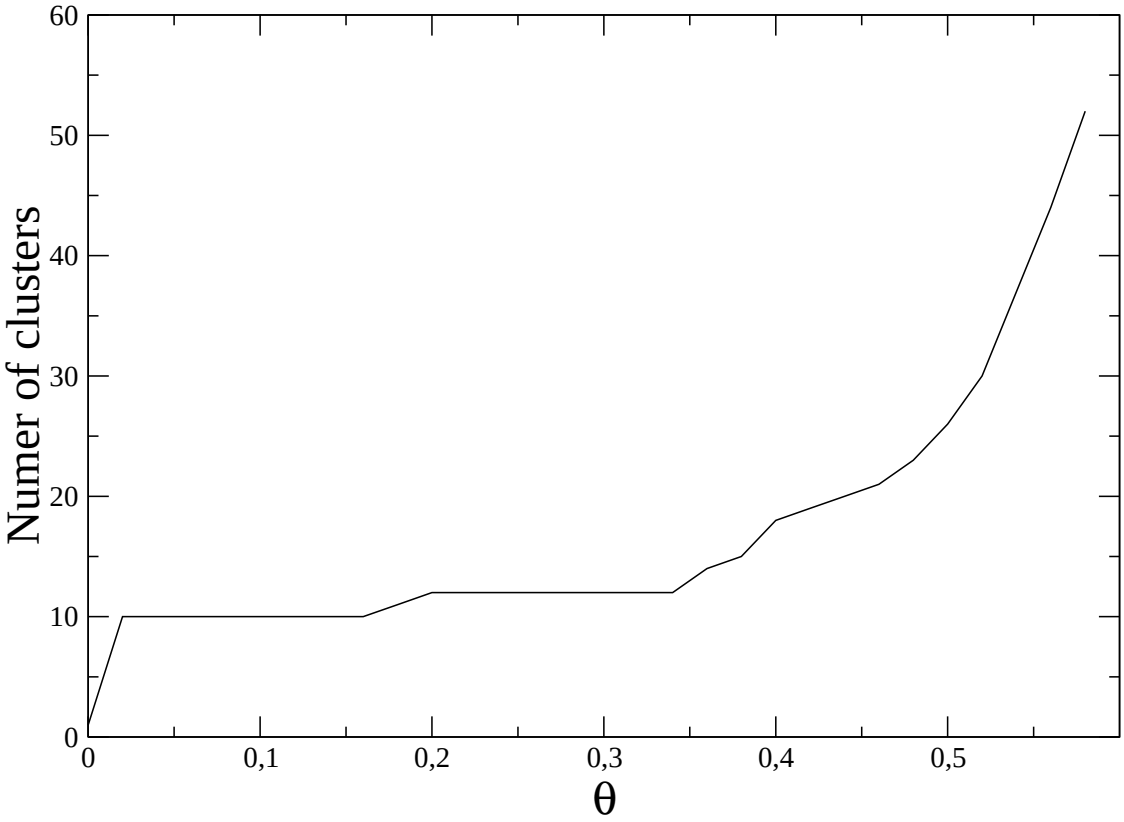

Figure 3.7: Typical dependence of the number of clusters in the parameter θ

Since on one hand the aim of the system is the correct identification of an unknown image, and on the other hand one has to check the functionality of this classification method by using known images in input, the only reasonable approach is to test the assignation given by the algorithm to an actually known image extracted from the database.
Within the CMC method approach, the ideal clustering result would be a pure dichotomic (or a three item system, if considering the border zone images apart from positive and negative image classes. In practice, the chaotic map system reaches a regime of good stability in the parameter θ (see figure 3.7) but with a number of clusters definitely greater than 2 or 3.

This behavior is given by several isolated point clusters corresponding to those images (positive) with "anomalous" feature values out of the average range, plus an unique big cluster containing all the rest of the points. At higher threshold values, the big cluster

breaks in smaller significant pieces grouping together mostly images of the same kind (positive or negative). The new partition is again stable with the variation of θ on a comprehensive range (in figure 3.7, the second stability range is $0.19 < \theta < 0.35$) and the non-trivial clusters are meaningful since one can associate them to a class with a simple majority rule (one must keep in mind that the assignation of all the points but one is known since the very beginning).

Within this framework, the final classification of the "unknown" image is given by the determined class of the cluster containing its representative point. If the image happens to be characterized by a set of "anomalous" features, the representative point will make a cluster on its own already for low stability range in θ: such an image can be safely labeled as positive. One may see here another slight difference with respect to the original CMC algorithm which assumes a one-to-one correspondence between clusters and classes: here it is compulsory to interpret the results in the light of problem's specificities.

The border zone images do not really count in the final clusters: with their contrasted features it is difficult to imagine how could they make an own cluster at this point (the situation has to be compared with the positive images which naturally group into clusters corresponding to their staining pattern feature characteristics).

The final assignation of the images is summarized in the table 3.2.

		Input class (medic diagnosis)		
		Positive	*Border zone*	*Negative*
Output class (CMC)	*Positive*	55	1	2
	Border zone	2	0	4
	Negative	9	2	15

Table 3.2: Confusion matrix: ground truth comparison with the CMC method classification, absolute values

The same results can be expressed in percents with respect to the input data class as in the table 3.3 below.

		Input class (medic diagnosis)		
		Positive	*Border zone*	*Negative*
Output class (CMC)	*Positive*	83 %	33 %	10 %
	Border zone	3 %	0 %	19 %
	Negative	14 %	67 %	71 %

Table 3.3: Confusion matrix: ground truth comparison with the CMC method classification, input percents

It has to be emphasized that due to the poor statistics these numbers are meant as a rough indication in the case of positive and negative images and an account of statistically irrelevant measured data in the case of the border zone images.

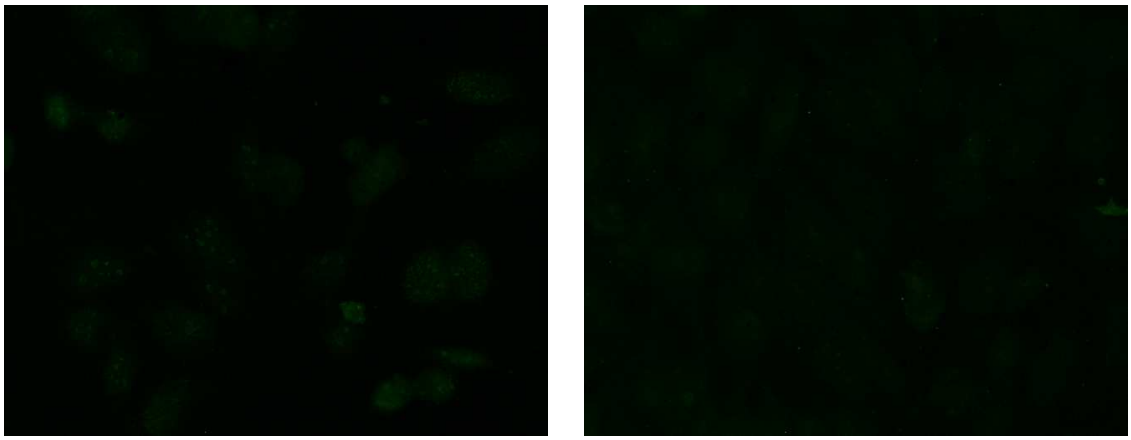

a) Nucleolar pattern b) Border zone nucleolar pattern

Figure 3.8: Samples of unrecognized nuclear staining patterns in the database

A rate of 83% successful recognition of **positive patterns** is fair in comparison with the ones reported for multiple configurations of a CAD system proposed in the literature [105].

The **negative image** correct classification rate of 71% might not look very impressive when compared with higher values in the literature, but it remains still fair compared to the bare 70% of [105] obtained by using only the multiple expert decision system with no rejection. Although it still looks somehow surprising that some negative images appear misclassified (since they form a rather homogeneous group), there are several potential explanations to this observational fact:

- the 6 groups of IIF images have been collected in different days under variable and highly influent conditions (mostly the timing, through the photobleaching of the fluorescent cells due to the incident light, but also the illumination conditions or the camera focus are important variable parameters) which cannot be completely compensated by the linear scaling of (3.1) and weigh upon the images features;

- the database limited size and distribution of the images (the negative images in the database are less than one third of the positives) constitute a natural bias towards positivity which cannot be completely compensated by automated weighing techniques;

- partially reflecting the preceding drawbacks, the feature system offers less discriminating power for the negative images, as shown in 3.2.2;

- the diffuse threshold between negative and border zone/positive images cannot exclude the possibility of erroneous image classification by the physician himself.

On another hand, for an automatic system it is by far more important to have an intensity fluorescence high recognition rate of the positive images than to have a high recognition rate for the negative images ([105]). This happens because of the following reasons:

- the primary interest of such an analysis is to not miss the positive cases (that is: to not discard potential pathology-revealing images by dismissing them as *false negatives*), while a *false positive* case has less engraving consequences (basically, if the label propagates up to the physician, it will cost him a couple of minutes to decide that the image should not be considered as positive);

- before becoming a final label, the image fluorescence intensity alleged positivity may be submitted to a cross-validation with an alternative scheme as in [105] and be dismissed during the pre-classification stage;

- even if a false positive survives to an eventual cross-validation step, the successive phase of cell staining pattern classification may rise a question mark if the image does not match the known patterns and dismiss it at this stage of the analysis.

From the preliminary analysis phase, since there was no clear discriminating feature between them and the other images, the **border zone images** were not expected to show up correctly; in fact, none of the three border zone images was actually classified as so. Four negative images and two positive images appear to the system as border zone, meaning only that the two modules (negative and positive classifiers) disagreed on them, not that they were judged to belong truly to that category for some pertinent characteristic. In other words, within this framework the border zone output represents nothing but an artifact of the chosen classification scheme.

Getting back to the **positive images**, for a deeper analysis, the different categories of cell staining patterns performed differently with the CMC algorithm (see table 3.4).

The best performance rate has been achieved by homogeneous and mixed patterns: there was no lost image characterized by these patterns. The cause relies in the peculiarities of the pattern itself: the homogeneous images bring full cell luminosity and are heavily marked by the feature contribution of the individual cells, while the mixed pat-

Input class	**Correctly classified**		**Incorrectly classified**	
	Cases	*%*	*Cases*	*%*
Speckled	20	80%	5	20%
Homogeneous	18	100%	0	0
Nucleolar	2%	29%	5	71%
Centromere	1	(50%)	(1)	(50%)
Mixed patterns	13	100%	0	0%

Table 3.4: Positive staining patterns recognition distribution

terns images bring more specific "positive" features and the images are well characterized overall.

With 80% of correct identification as positive, the speckled images are satisfactory recognized at this stage of the analysis, although for achieving realistic performance one should probably consider also the joint use of alternative classification systems in order to improve the rate.

A decisively bad performance despite the relatively poor numerical representation is displayed by nucleolar staining pattern images: with only 2 hits on a total of 7 images, these images meet serious difficulties to be recognized as true positives by the system used here. No complementary use of some alternative classification scheme could improve in a satisfactory way the inadequate effectiveness of the actual CMC algorithm implementation.

While exhibiting a quite low (50%) recognition rate, the centromere pattern should not be included in the present analysis for the following reasons:

- the number of images presenting this staining pattern is 2, absolutely insufficient for any pertinent conclusion (even a rough one);
- the centromere pattern image not recognized as positive is actually taken at a much higher dilution (1:2560 instead of 1:80) and has been considered here only for com-

parison purposes.

The overall rate of successful classification of the IIF images is given by the trace of the confusion matrix in table 3.2, that is around 78%. Unlike in most studies in the literature which refer to more populous and category-balanced selected databases, this efficiency characterizes roughly a database with image distribution typical for clinical practice IIF images output.

In order to circumscribe better the meaningfulness of the results obtained, an alternative classification approach in which the CMC algorithm was been replaced by an implementation of a KNN algorithm in the feature space has been proven on the same IIF image dataset. The nearest neighbor algorithm performed slightly worse, with an overall successful classification rate of 73% (66 images out of a total of 90). Practically all unsuccessfully recognized IIF images by the CMC method were missed also by the KNN classification scheme, which correctly labeled as negative just one image classified erroneously as border zone by the former algorithm. Conversely, the KNN-based algorithm misclassified four images correctly labeled by the CMC algorithm (one homogeneous and one speckled positive patterns were classified "border zone" as well as another negative image, while another speckled pattern positive image was classified negative). These results show that the method used here is at least as powerful as the alternative classification scheme depicted as exhibiting "the best performance in the current application" context ([105]).

3.3.2 Discussion

The chaotic map approach has been here considered as stand-alone method of classification of the fluorescence intensity of the IIF images, as generic overview and as a potential application for the future development of an automatic CAD system for the IIF images. The ultimate aim of such application is the eventual performance improvement over other systems already described and used in practice.

The CMC method has been here used both in a more "traditional" way (since it was possible to exploit the θ stability of the cluster number, unlike in the case of the mammographic images segmentation) and in a less conservative setting (since there was no one-to-one correspondence between clusters and IIF image classes and the associated class of a cluster had to be determined through a rule not pertinent to the CMC method itself).

The method led to positive results, comparable with the results provided by other methods on the same image database. Although a certain category of IIF images systematically did not display a good performance, the fact cannot be correlated to the method itself since another approach confirmed the poor ratings verified on this particular subset of positive nucleolar cell staining pattern images. It has to be emphasized however that any comparison with other performances quoted in the literature should be taken "as is" since it is flawed by a clear database bias; any definitive judgment should be formulated only on the solid ground of the results obtained on a public and statistically relevant IIF image database (which at present is still missing).

On the overall, the results are more than encouraging and seriously suggest the possibility of use of the CMC algorithm in an IIF image CAD workflow. The weaker points of the approach can be overcome with an appropriate combination with other systems and/or fine tuning of the parameters and of the feature system. It is safe to assert that a significantly larger database will make these operations feasible.

Conclusions

The chaotic map algorithm results to be an alternative enhancement method of the clustering of points in a data space with more orthodox approaches. The main conclusion of this work is that the chaotic map clustering has revealed his applicability in the analysis of biomedical images. As a general consideration, any kind of classification problem which can be formulated in terms of specific numerical features is potentially approachable with the algorithm. There are two types of difficulties one meets in the implementation of the algorithm:

- difficulties related to the statement of the problem in an appropriated form (choice of a model, selection of the relevant features, etc.), difficulties which are collateral and indirectly related to the algorithm itself;
- difficulties which arise from the very nature of the algorithm and are related to the type of output provided by the CMC algorithm or to the choice of an optimal set of parameters.

The algorithm has proven its robustness in two different classes of applications. While in the case of the mammographic images segmentation the results seem rather unimpressive, one has to keep in mind that the main cause of the apparently poor performance resides in the inherently tough task of constructing a "right" input for the algorithm, not in the algorithm itself. At present, there is no ultimate segmentation scheme through a system of features which does not incorporate any geometrical or shape-related characterization. Therefore, it is expected that *any* algorithm using this reduced system of features as an

input will produce less conclusive results.

Concerning the IIF images classification, the algorithm lead to fairly positive results even when applied on a rather limited database. In this occasion, the CMC approach has also shown its flexibility to cope with a situation slightly different with respect to its standard application flow. It is expected that the incorporation of a sensibly more important information by the extension of the database and a further fine tuning of all the parameters involved according to the statistically more relevant data will lead to a clear improvement of algorithm's performance. An immediate further application might be in this case the direct cell pattern classification, a task suiting even better algorithm's potentialities. The use of the algorithm in the IIF image classification task is an important step towards the improvement of the whole automatic analysis process and the objective standardization of the procedure.

As a final consideration, one should assert that although the CMC algorithm is undoubtedly robust and flexible, its practical applicability to a certain concrete problem cannot be determined a priori but has to be established from a case to another, by taking into account the situation specificity in all its aspects. Therefore, we advocate for the further practical use of the method in all the phases of IIF images classification, and we definitely support it as valid alternative to other clustering approaches for all the problems which can be modeled through a numerical feature dataspace.

Appendix A

Immunofluorescence Acronyms

AAB(s)	Autoantibody (-ies)
Ab(s)	Antibody (-ies)
ANA	Anti-nuclear antibody
CENP	Centromere Associated Protein
DIF	Direct Immunofluorescence
ELISA	Enzyme-Linked Immunosorbent Assays
FITC	Fluorescein isothiocyanate
HEp-2	Human Epithelial Cell (substratum)
Ig	Immunoglobulin (Antibody)
IgG	Immunoglobulin G
IIF	Indirect Immunofluorescence
IFT	Indirect Immunofluorescence Technology

Appendix B

IIF Images Features

In the subsequent definitions, $h(i)$ denotes the IIF image histogram value for the gray level $i\,(i \in \overline{0,255})$ while $im(k)$ denotes the gray level of the k^{th} point of the image.

0. **absolute maximum position**

$$f(0) = i_{max} \text{ such as } h(i_{max}) \geq h(j)\ \forall j \in \overline{0,255}$$

1. **histogram average value**

$$f(1) = \langle h(i) \rangle_i = \frac{\sum_{i=0}^{255} i \cdot h(i)}{\sum_{i=0}^{255} h(i)}$$

2. **histogram standard deviation**

$$f(2) = \sqrt{\langle (h(i) - \langle h(j) \rangle_j)^2 \rangle_i} = \sqrt{\frac{\sum_{i=0}^{255} (i - f(1))^2 \cdot h(i)}{\sum_{i=0}^{255} h(i)}}$$

3. **histogram third moment**

$$f(3) = \langle (h(i) - \langle h(j) \rangle_j)^3 \rangle_i = \frac{\sum_{i=0}^{255} (i - f(1))^3 \cdot h(i)}{\sum_{i=0}^{255} h(i)}$$

4. **histogram fourth moment**

$$f(4) = \langle (h(i) - \langle h(j) \rangle_j)^4 \rangle_i = \frac{\sum_{i=0}^{255} (i - f(1))^4 \cdot h(i)}{\sum_{i=0}^{255} h(i)}$$

5. **histogram range**

$$f(5) = i_M - i_m \quad \text{where} \quad h(j) = 0 \; \forall j < i_m \; \& \; \forall j > i_M$$

6. **first order entropy**

$$f(6) = - \sum_{\substack{i=0 \\ h(i)>0}}^{255} h(i) \cdot \ln h(i)$$

7. **number of relative maxima**

$$f(7) = \text{card}(M) \;\; \text{where} \;\; M = \{ i \mid h(i) - h(j) > 0 \;\; , \forall j \, , \;\; 0 < |j - i| < 5 \}$$

8. **energy around relative maxima**

$$f(8) = \sum_{i \in M} \sum_{\substack{j=i-4 \\ j \neq i}}^{i+4} (h(i) - h(j))^2 \;\; (M \text{ is defined as above })$$

9. **energy around absolute maximum**

$$f(9) = \sum_{\substack{j=i-4 \\ j \neq i_{max}}}^{i+4} (h(i_{max}) - h(j))^2 \;\; (i_{max} \text{ is defined as above, } i_{max} = f(0))$$

For the second order features, one defines four cooccurrence matrices corresponding to the four directions of first order neighbors (two on the diagonal, one horizontal and one vertical) in the original image. These matrices link the points according to the following rules:

coocE	image points (k) and $(k+1)$, if the latter exists and it is on the same image row with point (k) (the point at the right of (k))
coocS	image points (k) and $(k+w)$, w being the width of the image (in pixels), if point $(k+w)$ exists (the point under the point (k))
coocSE	image points (k) and $(k+w+1)$, if the latter exists and it is on the same image row with point $(k+w)$ (the point at the right of the point under (k))
coocNE	image points (k) and $(k-w+1)$, if the latter exists and it is on the same image row with point $(k-w)$ (the point at the right of the point over (k))

The matrix element is defined in the following manner:

$$coocE(m,n) = \frac{\operatorname{card} E(m,n)}{\sum_{p,q=0}^{255} \operatorname{card} E(p,q)} \quad \text{where} \quad E(m,n) = \{k \mid im(k) = m\,,\ im(k+1) = n\,,\ 0 \le m,n \le 255\}$$

and the analogous expressions for $coocS(m,n)$, $coocSE(m,n)$ and $coocNE(m,n)$.

All the features $10-19$ are obtained by computing the four feature values corresponding to the given directions (E, S, SE, NE) and averaging them.

10. **second order entropy**

    aproape inexistent

$$f(10) = -\sum_{\substack{m,n=0 \\ cooc(m,n)>0}}^{255} cooc(m,n) \cdot \ln cooc(m,n)$$

11. **second order contrast**

$$f(11) = \sum_{\substack{m,n=0 \\ cooc(m,n)>0}}^{255} cooc(m,n) \cdot (m-n)^2$$

12. **second order second angular moment**

$$f(12) = \sum_{\substack{m,n=0 \\ cooc(m,n)>0}}^{255} (cooc(m,n))^2$$

13. **second order inverse difference moment**

$$f(13) = \sum_{\substack{m,n=0 \\ cooc(m,n)>0}}^{255} \frac{cooc(m,n)}{1+(m-n)^2}$$

14. **second order correlation**

Let $hm1(m) = \sum_{n=0}^{255} cooc(m,n)$ and $hm1(n) = \sum_{m=0}^{255} cooc(m,n)$ (the marginals).

Let $hma1 = \sum_{m=0}^{255} m \cdot hm1(m)$ and $hma2 = \sum_{n=0}^{255} n \cdot hm2(n)$ (mean values)

$$f(14) = \sum_{\substack{m,n=0 \\ cooc(m,n)>0}}^{255} (cooc(m,n) \cdot m \cdot n - hma1 \cdot hma2)$$

15. **second order marginal means**

$$f(15) = hma1 \quad \text{defined as above}$$

16. **second order marginal standard deviations**

$$f(16) = \sqrt{\sum_{n=0}^{255} (hm1[n] \cdot n - hma1)^2}$$

17. **entropy of difference second-order histogram**

Let $hd(n) = \sum_{m=n}^{255} cooc(m-n,m) + cooc(m,m-n)$. Then:

$$f(17) = -\sum_{\substack{n=0 \\ hd(n)>0}}^{255} hd(n) \cdot \ln hd(n)$$

18. **difference second-order histogram angular moment**

$$f(18) = \sum_{\substack{n=0 \\ hd(n)>0}}^{255} (hd(n))^2$$

19. **difference second-order histogram mean**

$$f(19) = \sum_{\substack{n=0 \\ hd(n)>0}}^{255} hd(n) \cdot n$$

Bibliography

[1] M.G. Kendall – *Discrimination and classification,* In: P.R. Krishnaiah ed., Multivariate Analysis, 165-185, Academic Press, New York, 1966

[2] J. Moody, C. Darken – *Fast learning in networks of locally-tunned processing units* Neural computation, **1**, 281-294, 1989

[3] D.R. Tveter – *The Pattern Recognition basis of Artificial Intelligence* IEEE Press, New York, NY, 1998

[4] R.O. Duda, P.E. Hart, D.G. Stork – *Pattern Classification* 2nd ed. Wiley, New York, 2000

[5] A. Barbu, S.C. Zhu – *Cluster Sampling and Its Applications in Image Analysis* Department of Statistics Papers, Department of Statistics, UC Los Angeles, 2011 http://www.escholarship.org/uc/item/53b3v9b3

[6] C.D. Manning, P. Raghavan, H.Schütze – *An Introduction to Information Retrieval,* Cambridge University Press, 2008

[7] G. Getz, E. Levine, E. Domany – *Coupled two-way clustering analysis of gene microarray data* PNAS **97**(22) 12079-12084, 2000

[8] Y. Linde, A. Buzo, R.M. Gray – *An Algorithm for Vector Quantizer Design* IEEE Transactions on Communications, **28**, 8494, 1980

[9] T. Kosaka, S. Matsunaga, S. Sagayama – *Tree-structured speaker clustering for speaker-independent continuous speech recognition* In Proceedings of ICSLP. 1994

[10] P. Chiappetta, P. Colangelo, P. De Felice, G. Nardulli, G. Pasquariello – *Higgs search by neural networks at LHC,* Phys. Lett B **322**, 219, 1994

[11] A. Dekel, M.J. West – *On Percolation as a Cosmological Test,* The Astrophysical Journal *288*, 411, 1985

[12] L. Kullmann, J. Kertész, R. N. Mantegna – *Identification of clusters of companies in stock indices via Potts super-paramagnetic transitions,* Physica A **287**, 412, 2000

[13] A. Hutt, M. Svensen, F. Kruggel, R. Friedrich – *Detection of fixed points in spatiotemporal signals by a clustering method* Phys. Rev. E **61**:5, R4691-R4693, 2000

[14] A.K. Jain, R.C. Dubes – *Algorithms for Clustering Data,* Prentice Hall, Englewood Cliffs, NJ, 2000

[15] B.S. Everitt, S. Landau, M. Leese, D. Stahl – *Cluster Analysis* 5$^{\text{th}}$ ed., Wiley, 2011

[16] J.C. Gower – *A general coefficient of similarity and some of its properties*, Biometrics, **27**, 857-872, 1971

[17] P.-N. Tan, M. Steinbach, V. Kumar – *Introduction to Data Mining,* Addison-Wesley, 2004

[18] M. Blatt, S. Wiseman, E. Domany – *Super-paramagnetic clustering of data,* Phys. Rev. Lett., **76**, 3251-3254, 1996.

[19] M. Blatt, S. Wiseman, E. Domany – *Data Clustering Using a Model Granular Magnet,* Neural Comput., **9**, 1805-1842, 1997

[20] S.C. Manrubia, A.S. Mikhalkov – *Mutual synchronization and clustering in randomly coupled chaotic dynamical networks*, Phys. Rev. E Stat Phys Plasmas Fluids Relat Interdiscip Topics **60**, 1579-1589, 1999

[21] K. Kaneko – *Chaotic but Regular Posi-nega Switch among Coded Attractors by Cluster Size Variation*, Phys. Rev. Lett. **63**, 219-224, 1989

[22] K. Kaneko – *Clustering, Coding, Switching, Hierarchical Ordering, and Control in Network of Chaotic Elements*, Phys. Rev. Lett. **65**, 1391-1394, 1990

[23] K. Kaneko – *Partition Complexity in Network of Chaotic Elements*, J. Phys. A **24**, 2107-2119, 1991

[24] K. Kaneko – *Globally Coupled Circle Maps*, Physica D **54**, 5-19, 1991

[25] K. Kaneko – *Mean field fluctuation of a network of chaotic elements*, Physica D **55**, 368-384, 1992

[26] K. Kaneko – *Relevance of Clustering to Biological Networks*, Physica D **75**, 55-73, 1994

[27] K. Kaneko – *Information Cascade with Marginal Stability in a Network of Chaotic Elements*, Physica D **77**, 456-472, 1994

[28] K. Kaneko – *Remarks on the mean field dynamics of networks of chaotic elements*, Physica D **86**, 158-170, 1995

[29] E. Ott – *Chaos in Dynamical Systems*, 2$^{\text{nd}}$ ed., Cambridge University Press, 2002

[30] H.G. Schuster, W. Just – *Deterministic Chaos: An Introduction*, 4$^{\text{th}}$ ed. Wiley-VCH, 2005

[31] L. Angelini, F. De Carlo, C. Marangi, M. Pellicoro, S. Stramaglia – *Clustering Data by Inhomogeneous Chaotic Map Lattices*, Phys. Rev. Lett. **85**, 554 - 557, 2000

[32] C. Marangi, L. Angelini, F. De Carlo, G. Nardulli, M. Pellicoro, S. Stramaglia – *Clustering by inhomogeneous chaotic maps in landmine detection*, SPIE Proceedings Vol. 4170 (2001)

[33] R. Bellotti, F. De Carlo, S. Stramaglia – *Chaotic map clustering algorithm for EEG analysis,* Physica A, **334**, 222-232, 2004

[34] A. Tulipano, G. Donvito, F. Licciulli, G. Maggi, A. Gisel – *Gene analogue finder: a GRID solution for finding functionally analogous gene products,* BMC Bioinformatics **8,** 329, 2007

[35] N. Basalto, R. Bellotti, F. De Carlo, P. Facchi, S. Pascazio – *C*lustering stock market companies via chaotic map synchronization, Physica A **345**, 196, 2005

[36] N. Basalto, F. De Carlo – *C*lustering financial time series, In Practical Fruits of Econophysics: Proceedings of The Third Nikkei Econophysics Symposium; Takayasu, H. Ed. , Springer Verlag, Tokio, Japan, 2006

[37] L. Angelini, Dipartimento di Fisica, Università di Bari, Italy, Private communication, 2010

[38] R.V. Solé, S.C. Manrubia, B. Luque, J. Delgado, J. Bascompte – *Phase transitions and complex systems,* Complexity **1**(4), 13-26, 1996

[39] A. Meyer-Bäse – *Pattern Recognition in Medical Imaging,* Elsevier 2003

[40] J. Shi, B. Sahiner, H.-P. Chan, J. Ge, L. Hadjiiski, M. A. Helvie, A. Nees, Y.-T. Wu, J. Wei, C. Zhou, Y. Zhang, J. Cui – *Characterization of Mammographic Masses Based on Level Set Segmentation with New Image Features and Patient Information,* Med Phys. **35**(1): 280–290, 2008

[41] American Cancer Society, 2012 – *Cancer Facts & Figures 2012.* http://www.cancer.org/Research/CancerFactsFigures/ACSPC-031941 (accessed October 2012)

[42] K.C. Young, D.R. Dance – *Advances in X-ray mammography*, in *Breast Cancer*, M. Mitchell, R.H. Reznek, J.E. Husband eds., Cambridge University Press, New York, 2010

[43] B.C. Cavanaugh, S.McNally – *Mammography*, in *Breast Cancer Risk Reduction and Early Detection*, E.R. Sauter, M.B. Daly eds., Springer, 2010

[44] P.E. Freer, D.B. Kopans – *Screening for Breast Cancer: Mammography and Other Modalities*, in *Breast Cancer A Multidisciplinary Approach to Diagnosis and Management*, A.G. Taghian, B.L. Smith, J.K. Erban eds., Demos Medical Publishing, New York, 2010

[45] M. Samulski, R. Hups, C. Boetse, R.D.M. Mus, G.J. Den Heeten, N. Karssemeijer – *Using computer-aided detection in mammography as a decision support*, European Radiology **20** (10), 2323-2330, 2010

[46] P. Skaane, A. Kshirsagar, S. Hofvind, G. Jahr, R.A. Castellino – *Mammography screening using independent double reading with consensus: Is there a potential benefit for computer-aided detection?*, Acta Radiologica **53**:3, 241-248, 2012

[47] S. Ciatto, D. Cascio, F. Fauci, R. Ienzi, R. Magro, G. Raso, M. Vasile – *Computer assisted diagnosis (CAD) in mammography. Comparison of diagnostic accuracy of a new algorithm (CyclopusCAD®, Medicad) with two commercial systems.* La Radiologia Medica, **114** (4), 626-635, 2009

[48] M. Gromet – *Comparison of computer-aided detection to double reading of screening mammograms: review of 231,221 mammograms*, Am J Roentgenol. **190**, 854-859, 2008

[49] U. Bottigli, R.Chiarucci, B. Golosio, G.L. Masala, P. Oliva, S.Stumbo, D.Cascio, F. Fauci, M. Glorioso, M. Iacomi, R. Magro, G. Raso – *Superior Performances of the Neural Network on the Masses Lesions Classification through Morphological Lesion Differences* International Journal of Biomedical Sciences **1**, 56-62, 2006

[50] R.M. Nishikawa – *Computer-aided Detection and Diagnosis*, in *Digital Mammography*, U. Bick, F. Diekmann eds., Springer, 2010

[51] A. A. Farag, M.N. Ahmed, A. El-Baz, H. Hassan – *Advanced Segmentation Techniques* in *Handbook of Biomedical Image Analysis: Segmentation models Part A* – ed. J. S. Suri, D. L. Wilson, S. Laxminarayan, Kluwer 2005

[52] Z. Q. Wu, J. Jiang, Y. H. Peng – *Computational Intelligence on Medical Imaging with Artificial Neural Networks* in *Computational intelligence in medical imaging techniques and applications* eds. G, Schaefer, A.E. Hassanien, and J. Jiang, CRC Press 2009

[53] S. Tangaro, R. Bellotti, F. De Carlo, G. Gargano et al. – *MAGIC-5: an Italian mammographic database of digitised images for research* Radiologia Medica **113**, 477-485, 2008

[54] U. Bick – *Mammographic Signs of Malignancy: Impact of Digital Mammography on Visibility and Appearance*, in *Digital Mammography*, U. Bick, F. Diekmann eds., Springer, 2010

[55] Z. Ma, J.M. Tavares, R.N. Jorge, T. Mascarenhas – *A review of algorithms for medical image segmentation and their applications to the female pelvic cavity*, Comp. Methods Biomech. Biomed. Engin. **13**, 235-246, 2010

[56] D. Cascio, R. Magro, L. Vivona, F. Fauci, G. Raso, M. Iacomi, S. Sorce, M. Vasile – *A fuzzy logic application in clustering process on mammographic images*, Presented at the SPIE-IS&T Conference on Image Processing - Algorithms and Systems VIII, San Jose, CA, USA, 19-20 January 2010

[57] D.L. Pham, C. Xu. J.L. Prince – *Current methods in medical image segmentation*, Annual Rev. Biomed. Eng. **2**, 315-337, 2000

[58] G.B. Coleman, H.C. Andrews – *Image Segmentation by Clustering* Proc. IEEE Inst. Electr. Electron. Eng. **67**, 773-785, 1979

[59] L. Häberle et al. – *Characterizing mammographic images by using generic texture features*, Breast Cancer Research, **14**, R59:1-R59:12, 2012

[60] J.M. Jeske, J.R. Bernstein, M.A. Stull – *Screening and Diagnostic Imaging*, in *Atlas of Clinical Oncology – Breast Cancer*, D.J. Winchester, D.P. Winchester eds., B.C. Decker Inc., Hamilton · London, 2000

[61] M. Alvarez Benito, J. Camps Herrero, M. Sentis Criville, M. Martinez Galvez – *Breast Imaging*, in *Learning Diagnostic Imaging: 100 Essential Cases*, R. Riebs, A. Luna, P.R. Ros eds., Springer, Berlin/Heidelberg, 2008

[62] C.M. Appleton, K.N. Wiele – *Breast imaging cases*, Oxford University Press, New York, 2011

[63] R. Haralick, K. Shanmungam, I. Dinstein – *Textural features for image classification,* IEEE Trans. SMC-3 **6**(3), 610-621 1973

[64] R. Haralick – *Statistical and Structural Approaches to Texture*, Proc. IEEE Trans. Inst. Electr. Electron. Eng. **67**, 786-803, 1979

[65] A. Retico, P. Delogu, M. E. Fantacci, P. Kasae – *An Automatic System to Discriminate Malignant from Benign Massive Lesions on Mammograms,* Nucl. Instr. Meth. Phys. Res. 2006, A 569: 596-600

[66] K. Fukunaga – *Introduction to statistical pattern recognition,* 2nd edition, Elsevier 1990

[67] L. Zhao, E. E. N. Macau – *A network of dynamically coupled chaotic maps for scene segmentation*, IEEE Trans. Neural Networks 2001, **12**(6): 1375-1385

[68] A. Pikovsky, M. Rosenblum, J. Kurths – *Synchronization: a universal concept in nonlinear sciences*, Cambridge University Press, 2003

[69] H. Yousefi'zadeh, E.A. Jonckheere – *Neural Network Modeling of Discrete Time Chaotic Maps,* Technical Report, January 2002

[70] B. S. Marron – *Co-occurrence Matrix and Fractal Dimension for Image Segmentation,* arXiv:0908.4310v1 [stat.AP]

[71] *Biomedical image analysis and machine learning technologies: applications and techniques*, ed. F. A. Gonzalez & E. Romero, Medical Information Science Reference 2009

[72] W. Palma – *Long-Memory Time Series,* Wiley-Interscience 2007

[73] L. Angelini, M. Pellicoro, S. Stramaglia – *Phase Ordering in Chaotic Map Lattices with Additive Noise,* arXiv:cond-mat/0001444v1

[74] L. Kurz, M.H. Benteftifa – *Analysis of variance in statistical image processing,* Cambridge U.P. ,1997

[75] G. Chen. Y. Huang – *Chaotic Maps: Dynamics, Fractals, and Rapid Fluctuations,* Morgan & Claypool 2011

[76] M.A. Haidekker – *Advanced biomedical image analysis,* Wiley 2010

[77] X. Chen, X. Zhou, S.T.C. Wong – *Automated segmentation, classification, and tracking of cancer cell nuclei in time-lapse microscopy,* IEEE Transactions on Biomedical Engineering, **53**, 762-766, 2006

[78] R. Hiemann, N. Hilger, J. Michel, U. Anderer, M. Weigert, U. Sack – *Principles, methods and algorithms for automatic analysis of immunofluorescence patterns on Hep-2 cells.* in *Autoimmunity Rewievs*, p. 86, 2006

[79] R. Hiemann, N. Hilger, J. Michel, J. Nitscke, A. Bohm, U. Anderer, M. Weigert, U. Sack – *Automatic analysis of immunofluorescence patterns of Hep-2 cells,* Annals of the New York Academy of Sciences, **1109**, 358-371, 2007

[80] K. Huang, R.F. Murphy – *Automated classification of subcellular patterns in multicell images without segmentation into single cells,* in IEEE International Symposium on Biomedical Imaging: Macro to Nano, p.1139-1142, 2004

[81] P. Soda – *Early experiences in the staining pattern classification of Hep-2 slides,* IEEE Symposium on Computer Based Medical Systems, p.219-224, 2007, doi: 10.1109/CBMS.2007.42

[82] P. Soda, G. Iannello – *A multi-expert system to classify fluorescent intensity in antinuclear autoantibodies testing,* IEEE Symposium on Computer Based Medical Systems, p.219-224, 2006, doi: 10.1109/CBMS.2006.21

[83] U.S. Department of Health and Human Services National Institute of Allergy and Infectious Diseases – *Autoimmune Diseases*, NIAID web site, http://www.niaid.nih.gov/topics/autoimmune/Pages/default.aspx (retrieved December 2012)

[84] A. Fassano, T. Shea-Donohue – *Mechanisms of Disease: The Role of Intestinal Barrier Function in the Pathogenesis of Gastrointestinal Autoimmune Diseases*, Nature Clinical Practice: Gastroenterology and Hepatology **2**:9, 416-422, 2005

[85] S.P. Wheatley, Y.L. Wang – *Indirect immunofluorescence microscopy in cultured cells*, Methods Cell Biol. **57**, 313-332, 1998

[86] G.R. Burmester, A. Pezzuto – *Color Atlas of Immunology*, Thieme, Stuttgart · New York, 2003

[87] P.M. Bayer, B. Fabian, W. Hübl – *Immunofluorescence assays (IFA) and enzyme-linked immunosorbent assays (ELISA) in autoimmune disease diagnostics – technique, benefits, limitations and applications*, Scand J Clin Lab Invest Suppl., **235**, 68-76, 2001

[88] X. Bossuyt, S. Cooreman, H. De Baere, P. Verschueren, R. Westhovens, D. Blockmans, G. Mariën – *Detection of antinuclear antibodies by automated indirect immunofluorescence analysis*, Clin. Chim. Acta, **415**, 101-106, 2013

[89] N. Hahon, H.L. Eckert, J. Stewart – *Evaluation of cellular substrates for antinuclear antibody determination*, J. Clin. Microbiol., **2**, 42-45, 1975

[90] U. Sack, S. Knoecher, H. Warschkau, U. Pigla, F. Emmrich, M. Kamprad – *Computer-assisted classification of HEp-2 immunofluorescence patterns in autoimmune diagnostics*, Autoimmunity Rewievs **2**, 298-304, 2003

[91] U. Sack, K. Conrad et al – *Autoantibody Detection Using Indirect Immunofluorescence on HEp-2 Cells*, Annals of the New York Academy of Sciences **1173**, 166-173, 2009

[92] M.J. Fritzler – *Challenges to the use of autoantibodies as predictors of disease onset, diagnosis and outcomes*, Autoimmunity Rewievs **7**, 616-620, 2008

[93] R. Hiemann, N. Hilger, J. Michel, J. Nitschke, A. Böhm, U. Anderer, M. Weigert, U. Sack – *Automatic Analysis of Immunofluorescence Patterns of HEp-2 cells*, Annals of the New York Academy of Sciences **1109**, 358-371, 2007

[94] A.H. Coons, H.J. Creech, R.N. Jones – *Immunological properties of an antibody containing a fluorescent group*, Proc. Soc. Exp. Biol. Med **47**, 200-202, 1941

[95] A.H. Coons, M.H. Kaplan – *Localization of antigen in tissue cells. II. Improvements in a method for the detection of antigen by means of fluorescent antibody*, Journal of Exp. Med. **91**, 1-13, 1950

[96] R. Hiemann, T. Büttner, T. Krieger, D. Roggenbuck, U. Sack, K. Conrad – *Challenges of automated screening and differentiation of non-organ specific autoantibodies on HEp-2 cells*, Autoimmunity Rewievs **9**, 17-22, 2009

[97] A. Melegari, C. Bonaguri, A. Russo, L. Battistelli, T. Trenti, G. Lippi – *A comparative study on the reliability of an automated system for the evaluation of the cell-based indirect immunofluorescence*, Autoimmunity Rewievs **11**, 713-716, 2012

[98] I. Salamunić – *Laboratory diagnosis of autoimmune diseases new technologies, old dilemmas*, Biochemia Medica **20**, 45-56, 2010

[99] A. Kavanaugh, R. Tomar, J. Reveille, D.H. Solomon, H.A. Homburger – *Guidelines for clinical use of the antinuclear antibody test and tests for specific autoantibodies to nuclear antigens*, Archives of Pathology and Laboratory Medicine **124**, 71-81, 2000

[100] M. Haass, H.P. Lehmann – *New aspects of autoantibody detection with a new combination of autoantigenic targets*, Clinical and Applied Immunology Reviews **1**, 193-200, 2001

[101] K. Egerer, D. Roggenbuck et al. – *Automated evaluation of autoantibodies on human epithelial-2 cells as an approach to standardize cell-based immunofluorescence tests*, Arthritis Research & Therapy **12**, R40, 2010

[102] E. Cordelli, P. Soda – *Methods for greyscale representation of HEp-2 colour images*, CBMS '10 Proceedings of the 2010 IEEE 23rd International Symposium on Computer-Based Medical Systems, p. 383-388, 2010

[103] National Committee for Clinical Laboratory Standards – *Quality Assurance for the Indirect Immunofluorescence Test for Autoantibodies to Nuclear Antigen (IF-ANA): Approved Guideline*, NCCLS document I/LA2-A (ISBN 156238-311-6), Wayne, Pennsylvania, 1996

[104] A. Rigon, P. Soda, D. Zennaro, G. Iannello, A. Afeltra – *Indirect immunofluorescence in autoimmune diseases: Assessment of digital images for diagnostic purpose*, Cytometry **72B** p. 472-477, 2007

[105] P. Soda, G. Iannello, M. Vento – *A multiple expert system for classifying fluorescent intensity in antinuclear antibody analysis*, Pattern Anal. Applic. **12**, 215-226, 2009

[106] P. Soda – *Computer-Aided Diagnosis in Antinuclear Autoantibodies Analysis*, PhD thesis, Università Campus Bio-Medico di Roma, December 2007 Available online at: http://ilithia.unicampus.it/ilithia/DTDocumentiPDF/DT_1_SodaPaolo.pdf

[107] P. Soda, G. Iannello – *A Multi-Expert System to Classifying Fluorescent Intensity in Antinuclear Antibody Testing*, Proceedings of the 19$^{\text{th}}$ IEEE Symposium on Computer-Based Medical Systems, p.219-224, June 22-23, 2006

[108] T.G. Dietterich, G. Bakiri – /em Solving Multiclass Learning Problems via Error-Correcting Output Codes, Jour. Art. Int. Research **2**, 263-286, 1995

[109] E. Mayoraz, M. Moreira – /em On the Decomposition of Polychotomies into Dichotomies, Proc. Fourteenth International Conference on Machine Learning, Nashville, Tennessee, July 1997, p. 219-226

[110] L. Song, E.J. Hennink, I.T. Young, H.J. Tanke – /em Photobleaching kinetics of fluorescein in quantitative fluorescence microscopy, Biophysical Journal, **68**, 2588-2600, 1995